iScience

Article

Evaluating chemical effects on human neural cells through calcium imaging and deep learning

Graphical abstract

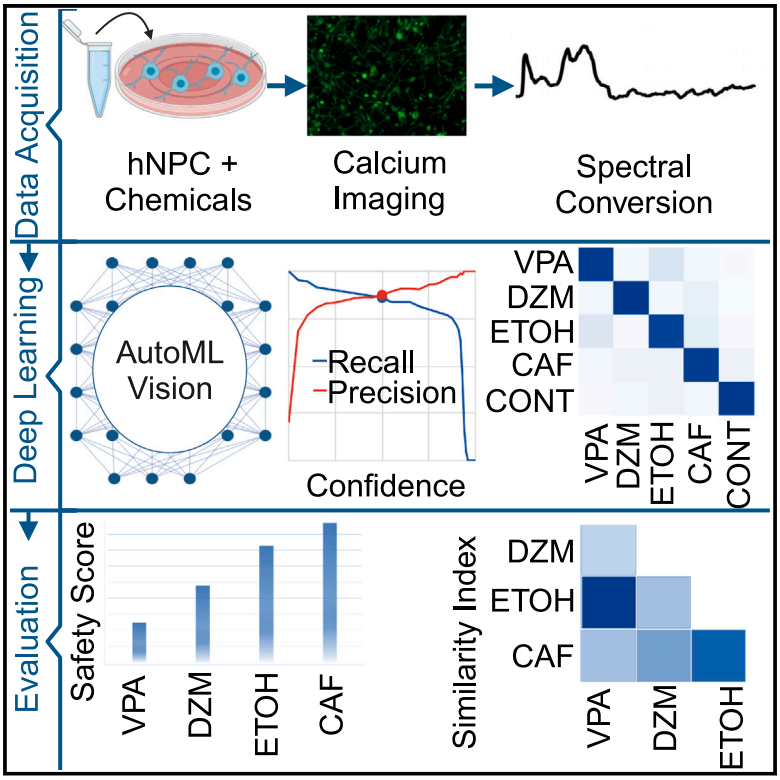

Highlights

- Deep learning of NPC calcium imaging predicts chemical impact on human neural cells
- Deep learning model predictions of chemical effect outperform traditional analysis
- ATP-stimulated calcium dynamics model shows higher accuracy than spontaneous dynamics

Authors

Ray Yueh Ku, Ankush Bansal, Dipankar J. Dutta, ..., Tomoki Uchida, Masaaki Torii, Kazue Hashimoto-Torii

Correspondence

abansal2@childrensnational.org (A.B.), mtorii@childrensnational.org (M.T.), KHTorii@childrensnational.org (K.H.-T.)

In brief

Biological sciences; Neuroscience; Machine learning

Ku et al., 2024, iScience *27*, 111298
December 20, 2024
https://doi.org/10.1016/j.isci.2024.111298

CellPress

iScience

CellPress
OPEN ACCESS

Article

Evaluating chemical effects on human neural cells through calcium imaging and deep learning

Ray Yueh Ku,[1,5] Ankush Bansal,[1,5,*] Dipankar J. Dutta,[1] Satoshi Yamashita,[1] John Peloquin,[1] Diana N. Vu,[1,4] Yubing Shen,[1] Tomoki Uchida,[2] Masaaki Torii,[1,3,*] and Kazue Hashimoto-Torii[1,3,6,*]

[1]Center for Neuroscience Research, Children's Research Institute, Children's National Hospital, Washington, DC 20010, USA

[2]Novel Business Development Department, Suntory Global Innovation Center Limited, 8-1-1 Seikadai, Seika-cho, Soraku-gun, Kyoto 619-0284, Japan

[3]Department of Pediatrics, Pharmacology and Physiology, School of Medicine and Health Sciences, The George Washington University, Washington, DC 20052, USA

[4]Present address: George Washington University School of Medicine and Health Sciences (SMHS), The George Washington University, Washington, DC 20052, USA

[5]These authors contributed equally

[6]Lead contact

*Correspondence: abansal2@childrensnational.org (A.B.), mtorii@childrensnational.org (M.T.), KHTorii@childrensnational.org (K.H.-T.)

https://doi.org/10.1016/j.isci.2024.111298

SUMMARY

New substances intended for human consumption must undergo extensive preclinical safety pharmacology testing prior to approval. These tests encompass the evaluation of effects on the central nervous system, which is highly sensitive to chemical substances. With the growing understanding of the species-specific characteristics of human neural cells and advancements in machine learning technology, the development of effective and efficient methods for the initial screening of chemical effects on human neural function using machine learning platforms is anticipated. In this study, we employed a deep learning model to analyze calcium dynamics in human-induced pluripotent stem cell-derived neural progenitor cells, which were exposed to various concentrations of four representative chemicals. We report that this approach offers a reliable and concise method for quantitatively classifying the effects of chemical exposures and predicting potential harm to human neural cells.

INTRODUCTION

The central nervous system (CNS) is highly susceptible to exposure to a variety of substances including alcohol, medications, chemicals in the environment, and even food additives.[1] New substances intended for human use or consumption must undergo extensive assessment for safety and toxicity before approval. Unique to the CNS is that, even if the overall cellular health is stable after exposure to a substance, behavioral abnormalities can occur through changes in neural function. Therefore, there is a critical need for an efficient platform for the initial assessment of pharmacological effects of various substances on neural cells (i.e., neurons, glia, and neural progenitor cells [NPCs]) prior to *in vivo* testing.

To investigate the effects of chemicals on neural cells *in vitro*, various assays for diverse indicators, including cell viability, morphology, and function,[2] have been developed. Electrophysiological recording is one such functional assay that has been applied to test the pharmacological and toxicological properties of test substances.[3] Although the patch-clamp recording technique has been used to accurately measure a variety of physiological characteristics of neurons and other cells, its low throughput nature has been an inevitable challenge.[4] Thus, higher-throughput techniques such as multielectrode array (MEA) recording and calcium imaging have attracted attention as alternative approaches.[5]

MEA allows simultaneous recording of electrical activities from multiple cells to evaluate neural networks[6,7]. Leveraging the scalability of MEA, several algorithms have been developed to extract features from extracellular recording data. These features are utilized in machine learning models for various applications, including the classification of neuronal cell types,[8] prediction of seizure probability by chemical exposure at different concentrations,[5] and detection of pathological cellular responses.[9] Popular classifiers employed with extracted MEA features include support vector machines (SVMs) and convolutional neural networks (CNNs). While novel feature extraction algorithms combined with these classical classifiers have enabled new insights, limitations of MEA technology include difficulties in recording intracellular electrophysiological dynamics and challenges in detecting heterogeneous activities among cells.[10] For instance, signals from a single cell have various manifestations depending on the distance of the electrode from the soma, but these are difficult to capture with MEA.

Calcium imaging, using sensing dyes or genetic tools, has been used as a method to directly observe heterogeneous

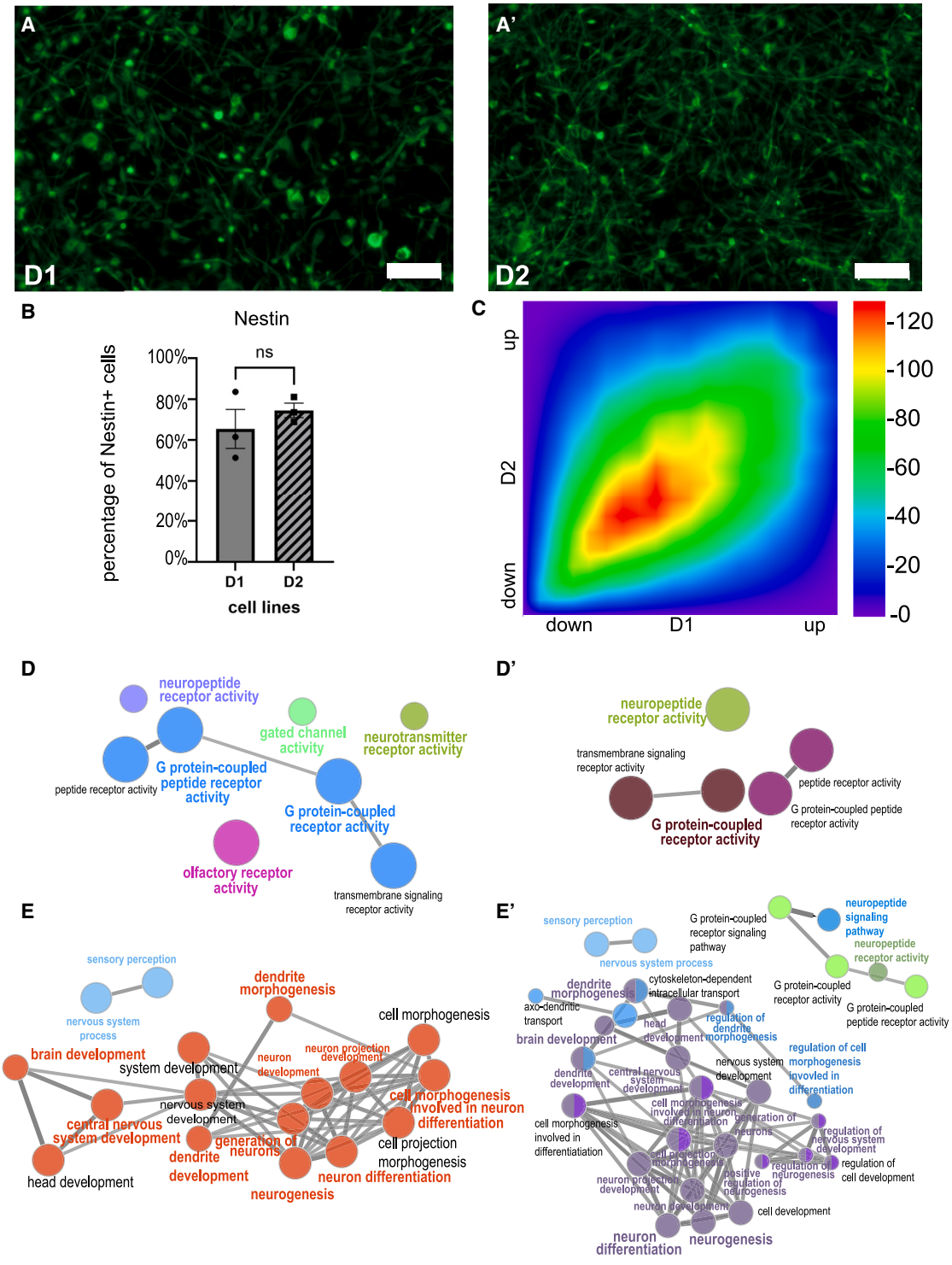

Figure 1. Characterization of human iPSC-derived NPCs used for calcium imaging

(A) Immunostaining for an NPC marker Nestin shows its expression in the majority of D1 (A) and D2 (A′) NPCs. Scale bar, 50 μm.

(B) The percentage of Nestin-positive cells were not significantly different between the two NPC lines (p = 0.4513 two-tailed t test). Data were presented as mean ± SD from three independent experiments.

(C) RRHO analysis between transcriptomes of D1 NPCs at passage 31 (x axis) and D2 at passage 14 (y axis). The colors denote log-transformed hypergeometric p values comparing the ranks of expressed genes, indicating a high similarity in gene expression ranks between the two datasets.

(legend continued on next page)

intrinsic activities of cells. Different patterns of calcium dynamics convey rich information that reflects the unique states of cell populations.[11,12] Calcium signaling is especially important for neural cells[13]; in addition to its essential roles in neuronal firing in mature neurons,[14] its proper levels and dynamics are crucial for various other cellular processes, including survival of neural progenitor cells,[15] neurogenesis,[16] and neuronal maturation.[17] To date, machine learning has been employed in various toolboxes to assist researchers in preprocessing calcium imaging data, including denoising and segmenting signals, and detecting spikes.[18–20] While a notable application by This et al. (2024)[21] demonstrated the utility of CNNs to predict T cell antigen specificity by analyzing calcium imaging data, the use of machine learning approaches to identify neuropathological conditions using calcium imaging data is still limited. While many previous studies employing calcium imaging have used cells from non-human species or human immortalized cell lines,[22–24] recent studies examining chemical effects have increasingly utilized cells and organoids differentiated from human induced pluripotent stem cells (iPSCs).[25,26] Since human neural cells exhibit species-specific characteristics that distinguish them from non-human cells commonly used in biomedical research,[27] the use of human neural cells may also be important in the assessment of chemical effects using calcium imaging data.

iPSCs are reprogrammed from somatic cells and self-renew in culture, and, by leveraging specific protocols, can be differentiated into various types of cells and tissues including NPCs and neurons.[28,29] Two major protocols have been developed to induce neurons from iPSCs. Transcription factor-driven differentiation involves forced expression of neural fate determinants like *Neurogennin2* (*Ngn2*) in iPSCs, rapidly driving their conversion into induced neurons (iNeurons) within 2–4 weeks.[30] However, only approximately 20 percent of cells differentiate into mature neurons with this protocol. Differentiation through NPC intermediates, on the other hand, involves a multi-stage process, beginning with embryoid body formation, induction of neuroepithelial cells, expansion of NPCs, followed by terminal differentiation over 6–12 weeks.[31] While direct programming is simpler and faster, the NPC approach allows scalable production of NPCs as an expandable intermediate, enabling banking of specific NPC lines.[28,29] iNeurons reach full functional maturity after 3 months in culture, while neurons differentiated with the NPC approach require 4 weeks for full maturation.[31,32] Neurons generated by either approach show heterogeneity in subtypes within the population.[33,34] However, electrophysiological recording and calcium imaging have been done without separating those iPSC-derived neuronal subtypes.[5,35–37]

In contrast to iPSC-derived postmitotic neurons, iPSC-derived NPCs are mitotic, allowing passaging *in vitro* for larger-scale studies. The electrophysiological properties of these immature cells are not fully equivalent to those of mature neurons (e.g., NPCs show higher resting membrane potentials and lower input resistance than mature neurons). Yet, excitability and expression of various ion channels as in mature neurons have been found in rat NPCs,[38] and delayed rectifier potassium channel currents have been shown in human iPSC-derived NPCs.[39] NPCs also exhibit neuron-like mitochondrial metabolism, with passive and active calcium activities similar to those in iPSC-derived neurons.[40,41] With these and other properties, iPSC-derived NPCs serve a useful model for the screening of drugs for neurological and psychiatric disorders.[40,42,43] Nevertheless, human iPSC-derived NPCs has not yet been tested as a platform of chemical screening combined with calcium imaging, although mouse NPCs have been tested for calcium imaging-based toxicology screening.[44] It is noteworthy that NPC-based analyses also provide insights into the effects of substances on the "developing" nervous system. As with iNeurons, cell type heterogeneity in iPSC-derived NPCs requires caution regarding the reproducibility of the analysis.[34]

To meet the growing demand for computational models for toxicity prediction, various models have been made publicly accessible.[45–47] These models enable prediction of several key drug properties such as Ames mutagenicity, skin sensitization, median lethal dose (LD50), drug-induced liver injury, and cardiac side effects with high accuracy.[48–52] Most of these models have been trained on datasets comprising more than 500 compounds and employed machine learning algorithms like random forests (RFs), SVMs, k-nearest neighbors (k-NN), graph neural networks (GNN), CNNs, and recurrent neural networks (RNNs) for binary classification.

In this study, we conducted a proof-of-concept study to predict the effects of chemicals on neural cells by building a machine learning model that requires minimal pre-processing of calcium imaging data obtained from human iPSC-derived NPCs. The performance of this machine learning model is compared with that of conventional statistical analysis of calcium dynamics measurements obtained by processing the same imaging data.

RESULTS

Characterization of human NPCs used in the analysis

Human NPCs possess several characteristics of mature neurons in such as gene expression, mitochondrial metabolism, and passive electrical properties.[39,53] They are thus suitable for rapid evaluation of how both neurons and progenitor cells in the nervous system respond to chemicals of interest without going through the time-consuming neuronal differentiation process *in vitro.* Considering the potential phenotypic variability among iPSCs from different individuals,[54] we utilized two well-characterized lines of NPCs that were differentiated from iPSCs originated from distinct donors (D1 and D2) in this study.

Immunocytochemical analysis confirmed the expression of a neural stem cell marker Nestin in 65.48% (±16.4%) and

(D) GO analysis of the transcriptome of D1 NPCs based on molecular functions (kappa score 0.4) shows the expression of genes relevant to neuronal functions, neurotransmitter receptors, neuropeptide receptor binding, and ion channel activities. (D′) Analysis of the D2 NPCs transcriptome similarly shows GO terms relevant to neuropeptide receptors.

(E) GO analysis of the transcriptomes of D1 (E) and D2 (E′) NPCs based on biological functions show the expression of genes involved in neuronal fate specification and commitment.

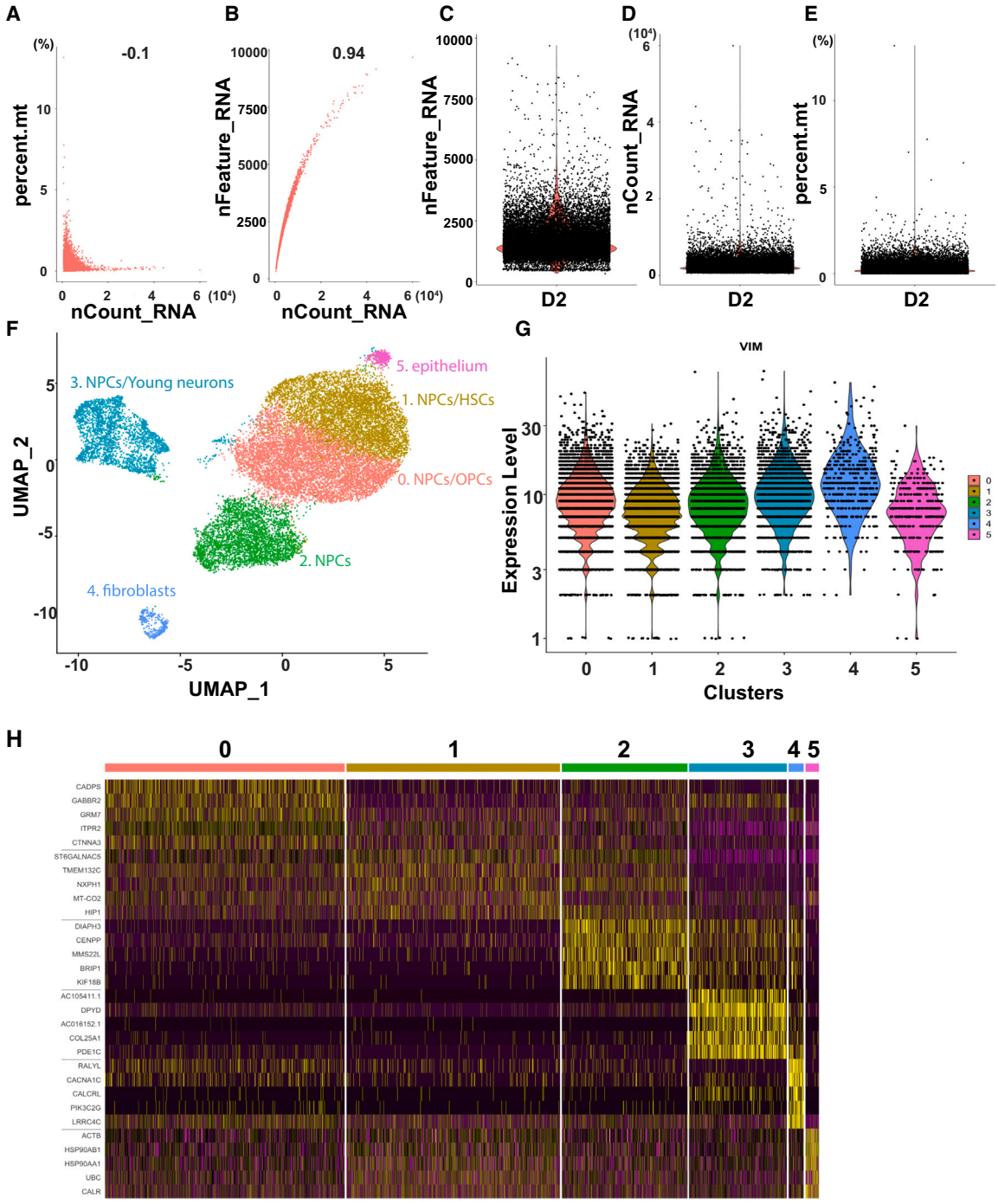

Figure 2. Molecular heterogeneity of NPCs in culture

(A) The scatterplot shows the percentage of UMIs assigned to mitochondrial genes in each cell (each dot represents a single cell). The X axis shows the total number of UMIs per cell. Cells with more than 5% of UMIs assigned to mitochondrial genes were excluded from further analyses.

(B) The scatterplot visualizes the number of genes detected in each cell. The strong correlation between total UMI counts (x axis) and detected gene numbers (y axis) affirmed the quality of data.

(C) The violin plot shows the distribution of the number of genes detected per cell. Outlier cells with fewer than 200 or more than 7,500 genes were excluded from downstream analyses.

(D) The violin plot shows the distribution of total UMI counts per cell. The median UMIs per cell was 9,969.

(E) The violin plot shows the distribution of the percentage of UMI counts from mitochondrial genes in total UMI counts per cell.

(legend continued on next page)

74.48% (±6.1%) of D1 and D2 NPCs, respectively (Figures 1A, 1A′, and 1B). Comparison of their bulk RNA sequencing (RNA-seq) data by the rank-rank hypergeometric overlap (RRHO) analysis showed similar molecular characteristics between D1 at passage 31 and D2 at passage 14 (Figure 1C), indicating that their molecular properties are stable over multiple passages. Gene ontology (GO) analysis of the same bulk RNA-seq data also showed that these NPCs express genes relevant to neuronal functions (e.g., neurotransmitter receptors) (Figures 1D and 1D′), consistent with previous reports.[55–58] Expression of genes linked to the activity of olfactory receptors (as defined by the GO classification) were also identified. While the expression of these genes also in the brain is known, their specific functions in the brain remain largely unexplored.[59] GOs associated with neural differentiation were found in both D1 and D2 transcriptomes as expected (Figures 1E and 1E′). Expression of vimentin, a marker for NPCs, was also found in both D1 and D2 NPCs at percentages comparable to Nestin-expressing populations in these NPCs (Figure S1). These results indicate that the molecular properties of these human iPSC-derived NPCs exhibit relevance to both NPCs and neurons, and remain stable through culture passages.

To examine cell-to-cell molecular heterogeneity in our NPC culture and to further assess the molecular identity of our samples, single nuclei RNA-seq of D2 NPCs was performed. Following multiple steps of quality control and filtering (Figures 2A–2E), the data were visualized by dimensionality reduction using Uniform Manifold Approximation and Projection (UMAP), which revealed that these NPCs were classified into six groups (Figure 2F). NPCs in each cluster showed a characteristic gene expression profile (Figure 2H). Cluster 0 included NPCs expressing both NPC markers and oligodendrocyte precursor cell markers, while cluster 2 included NPCs expressing only NPC markers. Cluster 1 included NPCs with some hematopoietic progenitor-like features. NPCs with features of young neurons were grouped in cluster 3. NPCs with fibroblast and epithelium features were found in clusters 4 and 5, respectively. While the feature-based clustering, thus, indicated the heterogeneity among NPCs in culture, the expression of an NPC marker vimentin was found in all clusters (Figure 2G), confirming their shared NPC characteristics.

Using two published RNA-seq datasets of multiple NPC lines (including D1 and D2), we performed Spearman's correlation analysis and confirmed that the two NPC lines have highly similar (Spearman's rank correlation coefficient: $\rho = 0.88$) transcriptomic profiles (Figure S2). Higher correlation coefficient of both D1 and D2 with other iPSC-NPC cell lines and the differentiated neurons indicate similar molecular properties (Figure S2).

Calcium dynamics in human NPCs exposed to different chemicals

To determine the validity of our approach, four well-characterized chemicals broadly consumed by humans[60–64] were tested. Valproic acid (VPA) is a branched short-chain fatty acid that blocks voltage-gated sodium channels, potassium channels, and L-type calcium channels. It also attenuates N-methyl-D-aspartate (NMDA)-mediated excitation, thereby being used for the treatment of epilepsy. Side effects of VPA intake include dizziness, headache, and drowsiness.[61] Ethanol (ETOH) is an organic chemical and has pleiotropic actions in the CNS, including inhibition of both voltage- and receptor-activated ion channels. Acute ETOH exposure elicits dizziness and nausea, followed by hangover symptoms that are generally unpleasant.[63] Diazepam (DZM) is a medicine of the benzodiazepine family and acts as an anxiolytic and sedative. It is also used for seizure treatments. Most of these effects are attributed to the facilitation of gamma aminobutyric acid (GABA) action, altering the electrophysiological activity of the brain.[64] Caffeine (CAF) is another organic chemical. It is a methylxanthine alkaloid known for its stimulating effect. High dosage of CAF triggers anxiety and headache. CAF induces calcium release from the cellular storage and blocks adenosine receptors.[65] It also functions as an antagonist for phosphodiesterase.[66]

Three test concentrations (high: H, medium: M, and low: L) for each of the four substances were set by considering pharmacokinetics determined in previous studies.[63,64,67–69] Concentrations used in *in vitro* toxicology tests are usually adjusted based on those measured in human plasma.[70,71] Therefore, we set the high concentrations at the blood concentrations at which adverse health effects such as reduced attention and fatigue were detected.[63,72–75] The medium concentrations of CAF and ETOH were set at the blood concentrations detected in normal daily consumptions in modern humans.[72,76,77] For DZM and VPA, the medium concentrations were set at the blood concentrations of clinically appropriate doses. The low concentrations were set at 5 (CAF, ETOH, and VPA) or 4 (DZM) times lower than the medium doses, same as the ratios of high doses to medium doses. NPCs that were exposed to the respective vehicle of each chemical served as controls.

Calcium imaging was performed at 1 Hz using a confocal microscope with or without stimulation (by ATP) for 300 s (Figure S3, Videos S1, S2, S3, S4, S5, and S6). Each chemical was tested using the two NPC lines (D1 and D2) in three or four independent experiments. For each cell line per experiment, randomly selected ten cells (or less when the number of cells responded is smaller than ten) that responded above the threshold level (see in STAR Methods) were used for analysis (Table S1). We first performed analysis using a conventional method (Figure 3A), measuring the six principal variables commonly used to characterize the pattern of calcium activities in neurons.[78] Since the calcium release (visualized by the change in fluorescence intensity of Fluo-4 calcium indicator) was mostly near the detection limit level in cultures without stimulation (Figure S3, Videos S1, S2, S3, S4, S5, and S6), the dynamics in calcium transients were analyzed using the data obtained in the ATP-stimulated condition. The six variables included the number of calcium

(F) UMAP visualization of the 6 clusters from 19,759 cells.
(G) Violin plots show high expression of an NPC marker, vimentin, in all cell clusters.
(H) The expression of each of the five genes most differentially expressed in each cluster compared to the other clusters is shown on the gene expression heatmap. Genes and cell cluster numbers are shown in rows and columns, respectively.

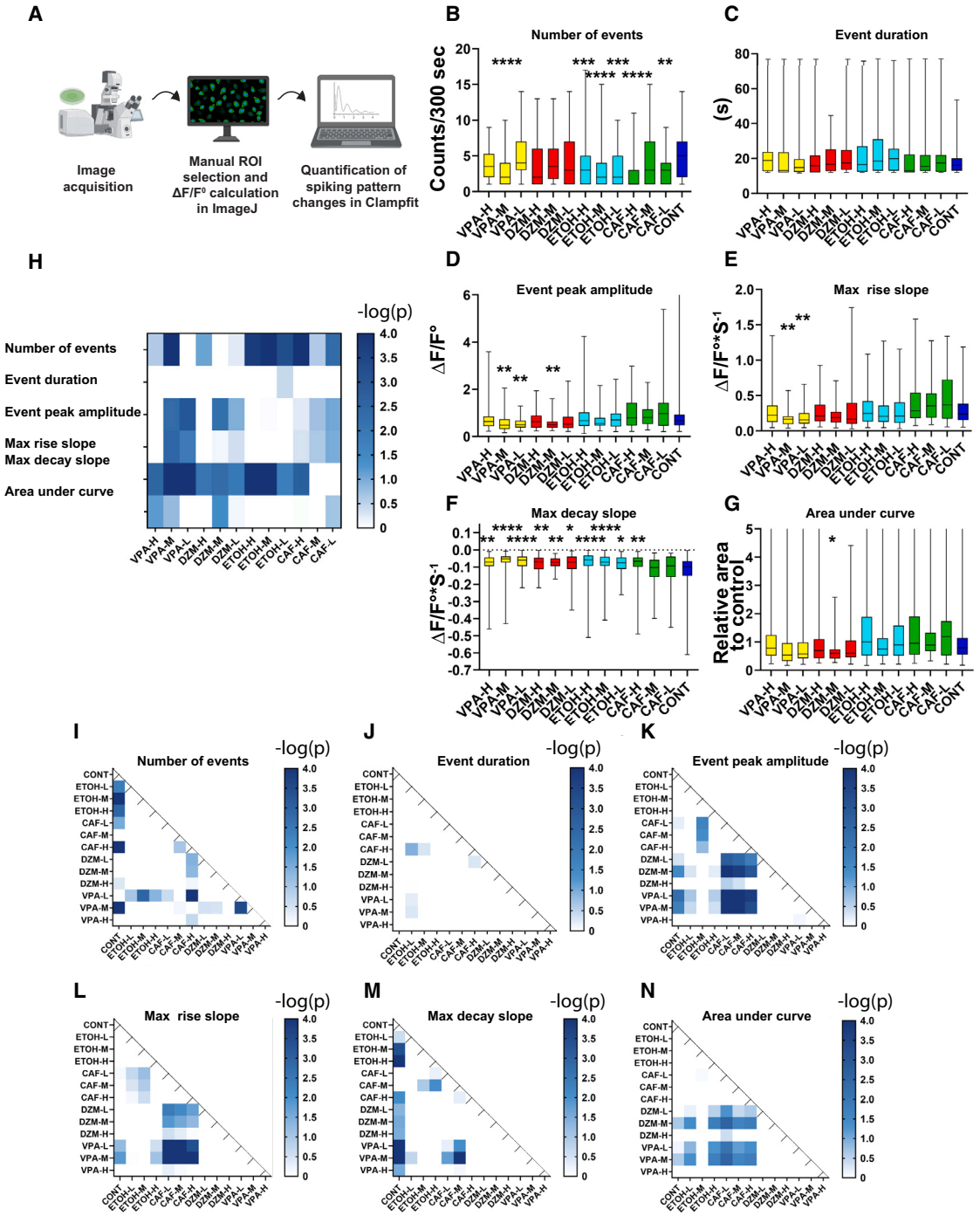

Figure 3. Kinetics of stimulated calcium transients are affected by exposure to chemicals

(A) Workflow of our analysis of calcium dynamics in human NPCs.

(B–G) Characterization of ATP-stimulated calcium transients in NPCs exposed to indicated chemicals at the high (H), medium (M), and low (L) concentrations, based on the number (B), duration (C), amplitude (D), max rise slope (E), max decay slope (F), and area under the plotted curve (relative to the value for CONT) (G). Non-parametric one-way ANOVA showed significant effects of chemicals ($p < 0.05$) in all measures. *, **, ***, and **** represent $p < 0.05$, 0.01, 0.001, and 0.0001, respectively, in comparison to CONT by post-hoc Dunn's test (mean ± SEM).

(H) Heatmap of negative log10-transformed p values from the Dunn's test performed in (B–G).

(I–N) Heatmaps of negative log10-transformed p values obtained by Dunn's test for pairwise comparisons of chemical's effects on each measure of calcium transients. Sample numbers are provided in Table S1.

spiking events in 300 s post stimulation (Figure 3B), mean values of duration (Figure 3C), amplitude (Figure 3D), max rise (Figure 3E), and decay slope (Figure 3F) of calcium spiking events detected in each cell, and the mean area under the calcium transient curve within the 300-s recording period (Figure 3G).[79] The change of fluorescence intensity (ΔF), which was normalized to the average signal during the first 5 s (F0) before ATP stimulation, was used to calculate the amplitude, max rise slope, and max decay slope (Figures 3D–3F). The area under the curve (AUC), which represents the amount of increasing calcium,[80] was quantified as the mean of values from all calcium spikes detected in each cell during the 300-s recording and converted to the ratio to the average AUC of the control (CONT) samples (Figure 3G).

The normality of data distribution was evaluated by D'Agostino-Pearson test for each of the six measures (Figure S4). The amplitude and the max rise slope were the only two measures that passed the normality test for most samples (Table S2). Consistent with the fact that both of the two measures are associated with the magnitude and rate of calcium release,[81,82] they showed similar patterns in the heatmap of *p* values in the comparison with the respective controls (Figure 3H). Significant reductions in these two measures were found in cells exposed to VPA at the low and medium concentrations (Figures 3D, 3E, and 3H). In many exposure conditions, the most significant changes were found in the number of spiking events and average max decay slope (Figures 3B–3F and 3H), while no significant effects were observed in the duration in all conditions (Figures 3C and 3H). The six measures also suggested that CAF at all tested concentrations had relatively milder effects on NPCs than the other chemicals (Figure 3H). Pairwise comparisons across all tested conditions (Figures 3I–3N) showed that all chemicals had little effects on the mean duration of spikes (Figure 3J). VPA and DZA showed a similarity in their difference from CAF in the amplitudes, max rise slope, and AUC (Figures 3K, 3L, and 3N).

Machine learning of calcium dynamics for the classification of chemical effects on human NPCs

Analysis of the six principal measures extracted from the plotted calcium transients loosely pointed out the differences and similarities between the effects of different chemicals and concentrations on human NPCs. However, much of the information is inevitably lost from the raw data with this approach. The interpretation on the differences and similarities may also become arbitrary. To address this issue, we developed a deep learning model that allows analyzing acquired images of calcium activities without extracting to a few selected principal variables. To generate input data for deep learning, ΔF/F0 traces of individual cells were plotted using the MATLAB GUI described in Romano et al. (2017).[83] The same data as we used in the analysis with six principal variables were used. These calcium transients plotted over 300 s were formatted as image data of 875 × 675 pixels per cell (Figure 4A). These images were then assorted based on exposure conditions (i.e., chemicals and concentrations) (Figures 4B and 4C). The number of images used in this study is listed in Table S3.

Prior to testing the performance of machine learning models, input data were visualized using t-distributed stochastic neighbor embedding (t-SNE) (Figure 5A). With various combinations of a perplexity value (5–500), iteration for dimensionality reduction of the single-cell trace data (1000–5000), and other parameters (see STAR Methods section), the size of clusters did not change significantly; although calcium imaging data from ATP-stimulated cells exposed to the high concentrations of chemicals were segregated from the others, the overall presence of many small clusters indicated large variability within the data for each exposure condition. In addition to higher correlation of gene expression (Figure S2), no separable clusters between D1 and D2 cell lines in t-SNE of calcium trace data suggest non-separable characteristics between cell lines.

Traditional machine learning algorithms, such as RF,[85,86] excel in interpretability and are less prone to overfitting, but may not be as effective as child (CNNs in handling complex image datasets.[87,88] Gradient boosting (GB)[89–91] works well on both structural and unstructured data. It is capable of mitigating overfitting, but struggles with feature extraction from complex image data.[92–94] SVMs[95] are interpretable, less prone to overfitting, and effective for classifying low-dimensional and structured data.[96,97] However, SVMs require feature engineering, such as kernel selection, and face scalability issues as the complexity of dataset increases. Decision trees (DTs)[98] are interpretable and easy to implement and do not require normalization or scaling, making them suitable for certain types of datasets. However, they are not well suited for high-dimensional image datasets and tend to overfit if the tree is deep or datasets are small.[93,99] The neural architecture search (NAS) in Google Automatic Machine Learning (AutoML) uses an RNN or the controller that controls the building of different CNN architectures, which are then trained and tested for performance (Figure 4D).[84] The controller consists of an arbitrary number of normal convolution cells (Figure 4E) and a reduction cell (Figure 4F). It iterates this process over thousands of epochs, learns from the performance of the trained child CNN in each epoch, and outputs a final CNN architecture optimized for classification of the dataset, with minimal overfitting and underfitting tendencies. Deep neural networks, such as CNNs, perform well on visual inputs in their classification, but their hyperparameter optimization is largely empirical process. CNNs also have limited interpretability.

To select an algorithm that is most suitable for processing our datasets, we compared the performance of several different algorithms described previously on the image datasets of ATP-stimulated calcium transients in NPCs exposed to the four chemicals at the high concentration. Each image dataset was split randomly into the data used for training, validation, and testing (Table S4). The precision, recall, and F1 scores (see details in STAR Methods) showed that AutoML Vision performed best on our particular datasets (Table S5). Therefore, we selected AutoML Vision for further applications.

To compare early stopping function and manual determination of training duration in AutoML Vision, precision and recall values obtained using early stopping (training was terminated at ~64 node hours via its built-in hyperparameter optimization function) were compared with those obtained through the training terminated at 16 and 40 h (Figure S5). A total of 1,244 images of calcium transients (in ATP-stimulated condition) from NPCs exposed to each of the four chemicals at the high concentrations or from controls (NPCs without chemical exposure in the same

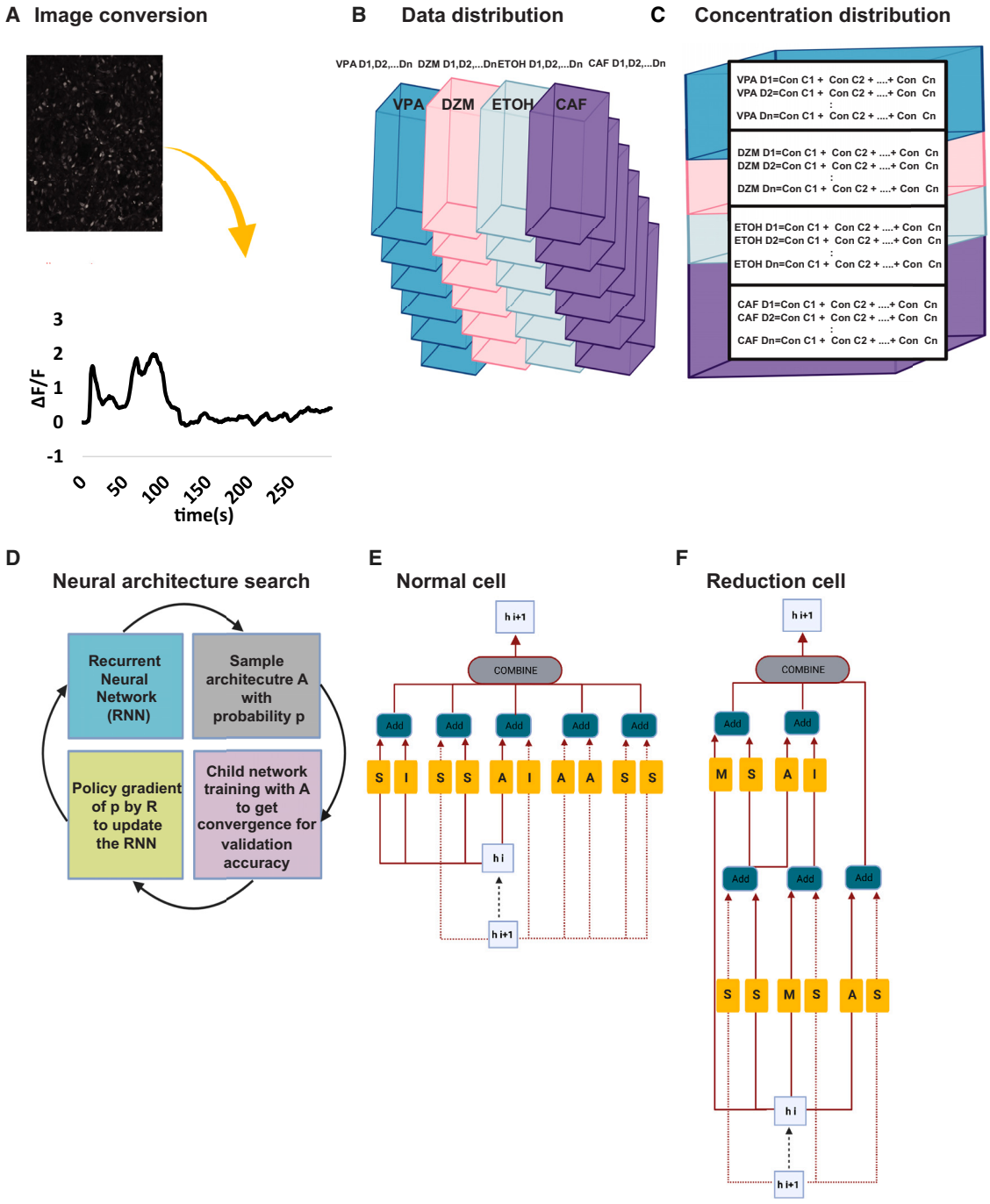

Figure 4. Workflow of Google Automatic Machine Learning (AutoML) Vision analysis

(A) The data assortment section includes multiple layers. 1 Hz image series for 300 s after stimulation are converted to a trace of relative fluorescence intensity change.

(B and C) Approximately 1,200 traces are generated per culture dish. Trace image data are assorted into 4 groups of different chemicals (B) that include 3 concentrations and 1 experimental control (C). Two biological replicates are included for each concentration.

(D) Google AutoML Vision uses neural architecture search (NAS) algorithm (adapted from the study by Zoph et al.,[84] see details in STAR Methods) by identifying architecture A using recurrent neural network (RNN) with the probability p. Child network with the given A is set for training to achieve the accuracy R.

(E and F) Structures of normal (E) and reduction (F) cells (adapted from the study by Zoph et al.[84] Each white box (labeled h i) shows a hidden state from the previous activation and the gray oval shows the output of combining different operations for pooling using softmax function: separate (S), identity (I), and average (A). In the reduction cell, maximum (M) operator is also used for pooling. Each block results in convolutional cells by primitive operators shown in yellow and combination operations shown in green.

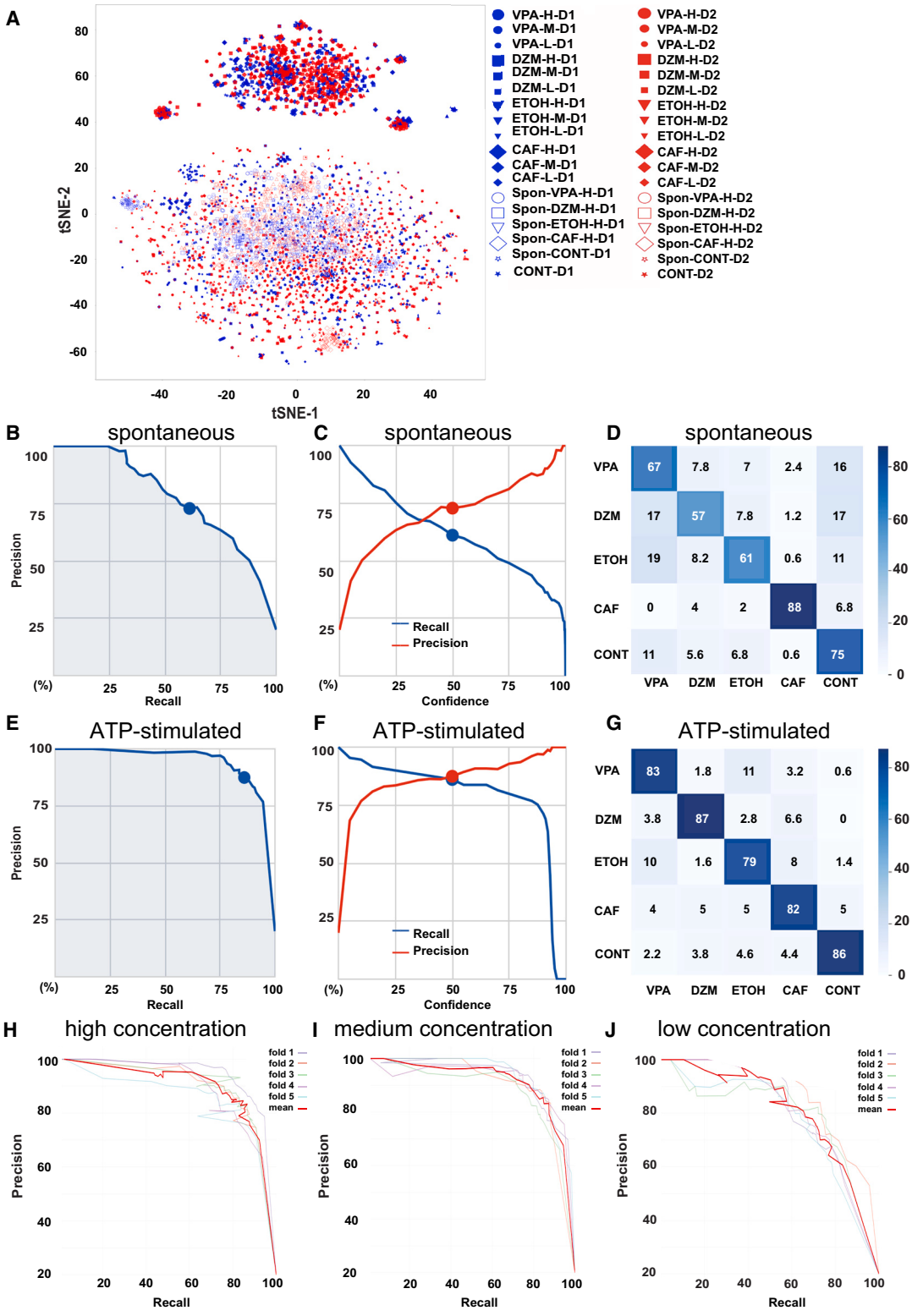

Figure 5. Machine learning of temporal traces of calcium activity

(A) t-SNE analysis of 4,275 images of temporal trances of calcium activity from indicated groups. Some high concentration samples form clusters that are unrelated to the type of chemical. Using different settings (e.g., perplexity value: 5–500, iteration: 1000–5000) provided similar output maps.

(legend continued on next page)

experimental lots) were used. 16 node hours were insufficient for training as evident from the precision-recall curve and confidence score (Figure S5A). No significant differences were observed between scores of model performance obtained through the training terminated at 40 h and early stopping (Figure S5A). Next, we checked input sizes. The precision, recall, and F1 scores were similar between the models with input sizes of 50, 200, and 1,000 images randomly selected from the entire image dataset for model training, indicating that 50 images as input was sufficient for establishing model (Figure S5B).

We next compared the prediction performance between high-concentration models trained with the datasets of spontaneous (Figures 5B–5D) and ATP-stimulated (Figures 5E–5G) calcium activities as input. Area under precision recall curve (AUPRC) (Figures 5B and 5E), confidence interval (CI) (Figures 5C and 5F), confusion matrix (Figures 5D and 5G), as well as the precision, recall, and F1 scores (Table S5) indicated that the model trained with the dataset of ATP-stimulated calcium activity outperformed that trained with the dataset of spontaneous calcium activity. 5-fold cross-validation of the models trained with datasets of ATP-stimulated calcium activity at the three (H, M, and L) different chemical concentrations was then performed. The AUPRC indicated that the models with datasets of the high and medium concentrations classified chemicals more accurately (Figures 5H and 5I) than the model with a dataset of the low concentration (Figure 5J).

Based on the results aforementioned, the ''safety score'' was calculated to determine the applicability of our deep learning model to quantitatively assess the risk of chemicals on neural functions (Figure 6A); to obtain the safety score, the percentages of false negatives (FNs) (i.e., exposure to the chemical of interest is recognized as the control exposure) from the 5-fold cross-validation were averaged and weighted according to the concentration of chemicals (L, M, and H) (see STAR Methods for the formula). These safety scores showed that the order of risk levels for the four chemicals tested (Figure 6A, high to low risks: VPA, DZM, ETOH to CAF) fits well with previous reports and general knowledge,[73,100–104] as well as with our results using conventional six principal measures (Figure 3) that predicted weakest effects of CAF on neural activities.

The ''similarity matrix'' was also calculated to predict the similarity between the effects of different chemicals on neural functions, utilizing the percentages of false positives (FPs) and FN (i.e., exposure to a chemical of interest is recognized as exposure to the other) obtained in the 5-fold cross-validation for each chemical (Figure 6B). The similarity matrix indicated the highest similarity between VPA and ETOH among the other comparisons, consistent with their classification by the ChemMine tools[105] as having similar physiochemical properties (Figure S6), although their similarity was not evident in our results obtained by the conventional method using six principal measures from calcium transient (Figure 3).

DISCUSSION

This study provided proof-of-concept showing deep learning model with calcium dynamics traces in human iPSC-differentiated NPCs as an efficient approach to determine if a chemical of interest may interfere neural activity, without the need of categorically extracting and analyzing multiple features of calcium transients. It thus carries potential that may be used in conjunction with other toxicology screening tools for multi-faceted, meticulous evaluation of novel chemicals.

2D cultures of human iPSC-derived NPCs with high sensitivity to toxins and various substances[106–109] offer a suitable (e.g., easy handling, short culture time before testing, and scalability) platform for screening chemicals. However, as with many *in vitro* systems, simple NPC cultures lack complex cell-to-cell interactions as seen *in vivo* and influences from other tissues and organs that metabolize those chemicals. For example, acetaldehyde, a metabolic intermediate of ethanol generated in the liver, has been suggested to affect the CNS,[110,111] but such effects are omitted in our cultures. Yet, our results demonstrate that cultures of human iPSC-derived NPC provide effective and efficient means of early prediction of potentially harmful substances to human neural cells.

Calcium imaging data from human NPCs exposed to representative chemicals, VPA, ETOH, DZM, and CAF, were analyzed in two ways: the conventional approach focusing on representative variables and the deep learning approach that directly analyzes calcium dynamics in minimally processed data. Both approaches worked to reveal the similarities and differences between the effects of exposure to different chemicals. The analysis of the six properties of plotted calcium transients in NPCs (Figure 3) provided results that were consistent with previous reports using different cell types; it has been shown that CAF induces calcium release in sensory neurons in the retina and dorsal root ganglia,[112,113] and increases spike amplitudes and decay slopes in NMDA-stimulated embryonic retinal cells,[114] while exposure to VPA and DZM has been shown to reduce spontaneous calcium activity in various types of cells.[115–117] Our results of ATP-stimulated calcium activities in NPCs similarly showed the differential effects of CAF and VPA/DZM in several measures, including the peak amplitude, maximum rise slopes, and AUC (Figures 3D–3F, 3G, 3K, 3L, and 3N).

An advantage of the deep learning approach is its scalability by directly handling complex, large single-cell calcium transient data without additional extraction of limited properties. While the conventional method was able to predict that VPA and DZM differ from CAF to the same extent among the four chemicals (Figure 3), it would be challenging to make similar predictions in a larger scale screenings. Another caveat of the conventional approach is that, for many of the quantified parameters, the strength of effect of each chemical does not simply correlate to its concentration. As we did not observe cell deaths or obvious

(B–G) Precision-recall curves of the best model (B, C, E, and F) and averaged confusion matrices shown as percentages (D and G) from 5-fold cross-validation. These were generated using AutoML Vision trained with images of temporal traces of spontaneous (B–D) and ATP-stimulated (E–G) calcium transients in NPCs exposed to each chemical at the high (or control) concentration. The numbers of image datasets of spontaneous and ATP-stimulated activities were 1,457 and 1,244, respectively.
(H–J) 5-fold cross-validation of the models trained with ATP-stimulated datasets of the high, medium, and low concentrations.

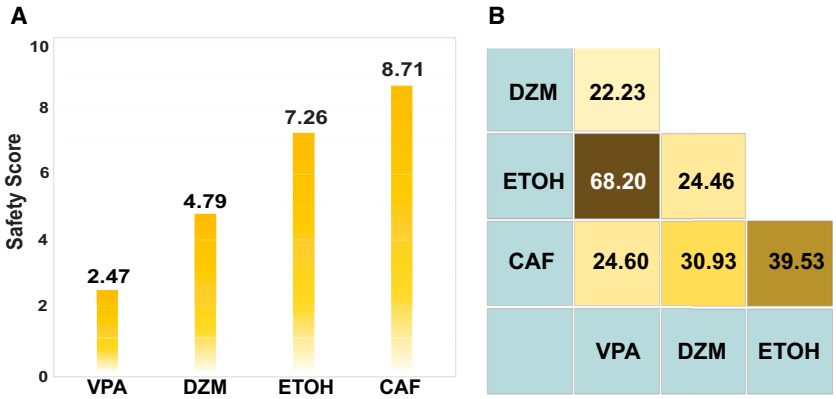

Figure 6. Safety and similarity of chemical effects on NPCs predicted by machine learning

(A) Safety scores predict the order of safety levels for the four tested chemicals.

(B) The similarity matrix predicts the similarities between the effects of the four tested chemicals on neural functions.

health issues in NPCs during recording in any tested conditions, these factors are unlikely the primary causes of this inconsistent concentration dependency. One possible cause of this inconsistency may be that the output of chemical's effects in calcium spikes increases variability over the period of recording. Large variabilities were particularly evident in the duration of a spike and the mean AUC ratio (Figures 3C and 3G). Measuring only on the first few spikes instead of calculating the means of all detected spikes in the 300-s recording period after stimulation may provide more consistent concentration-dependent results.

The results obtained by our deep learning model corroborate those obtained by the conventional approach. For example, as the six measures suggested that CAF had only mild effects on calcium transients compared to the other chemicals (Figure 3), the safety score predicted the highest safety of CAF (Figure 6A) and the confusion matrix showed the largest false classification of CAF as the control among the four chemicals tested (Figure 5G). The safety scores also ranked VPA and DZM as the first and second highest risk chemicals (Figure 6). Similar results have been reported in a large-scale ranking of prescribed drugs based on their risk of causing liver injury in clinical cases[118]; albeit for non-neural tissue, CAF ranked in the safest category, while DZM was in the middle and VPA in the high risk group (ETOH was not included in the study). A notable feature revealed by machine learning, but not by the conventional method (Figure 3), is the highest similarity between ETOH and VPA among the tested substances (Figure 6B). This is consistent with their similarity in chemical properties predicted by ChemMine tools (Figure S6). Regarding their biological effects, both ETOH and VPA are known to induce neural tube defects by interfering fetal folate metabolism.[119] ETOH has also been found to potentiate the anticonvulsant effects of VPA.[120] Thus, the safety score and the similarity matrix serve as useful indices to express overall similarities and differences in the effects of different chemicals on the nervous system.

Although it is beyond the scope of this study to identify specific molecular mechanisms by which different chemicals have similar or different effects on the calcium transients in NPCs, there are several potential pathways. One common target affected similarly or differently by the four chemicals is GABA signaling. VPA inhibits GABA degradation by reducing the expression of GABAA receptors in the membrane,[121] decreasing GABAergic inhibition, while DZM enhances GABA potentiation by directly binding to GABAA receptors and augments GABA signaling.[122–125] ETOH directly binds to GABAA receptors,[126] while indirectly affects GABAB receptors.[127] As such, ETOH increases presynaptic release of GABA[128] and the amplitude and decay prolongation of GABAA-receptor-mediated inhibitory postsynaptic potentials (IPSPs).[129–131] ETOH also regulates GABA signaling by inducing brain steroidgenesis or via corticotrophin releasing factor, CRF1.[130,132] CAF, on other hand, increases the release of GABA via binding to adenosine receptors.[113,133–135]

Similarities in the pharmacological effects of VPA and ETOH have also been shown in the inhibition/reduction of histone deacetylases (HDACs), a class of enzymes that regulate the expression and activity of numerous proteins. VPA is a universal inhibitor of HDAC, while the inhibitory effect of ETOH is observed in the amygdala.[136,137] Upregulation of heat shock protein 70 (HSP70), a highly conserved molecular chaperone that plays critical roles in protein homeostasis, is another commonly observed cellular response to VPA and ETOH.[138,139] Induction of *hsp-70* mRNA expression by CAF has also been shown in *C. elegans* and zebrafish.[140,141] In contrast, inhibition of HSP70 by DZM in the brain has been reported in multiple species.[138,142] It is thus clear that similar/different effects of these chemicals are attributed to the regulation of a wide variety of molecular pathways, not just a few. Elucidating the molecular mechanisms by which various chemicals exert similar and different effects on neural cells warrants future research.

Limitations of the study

The approach demonstrated here is intended for rapid and sensitive functional screening of chemicals based on their effects on neural cells. While this study provides proof-of-concept for the evaluation of chemical effects on neural cells through calcium imaging and machine learning, focusing on four chemicals, to increase the predictive power, accuracy, and validity of our approach, the training data will need to be expanded to include a broader, if not exhaustive, selection of substances. The four chemicals were tested by acute exposure at three different concentrations based on physiological or therapeutic concentrations. However, in clinical overdose cases, higher blood concentrations of VPA or DZM have been reported.[74,75] Therefore, it would also be important to test at a wider range of concentrations, as in the study on the prediction of epileptic activity using machine learning of MEA datasets obtained at six different chemical concentrations.[5] Testing the applicability of machine

learning models to the assessment of the effects of long-term chemical exposure would be another important direction of research. Automation of cell culturing, chemical treatment, and calcium signal recording would allow for more efficient protocols.[143–145]

Beyond the development of simplistic chemical effect prediction models, such as the one presented in this study, lies the challenge of predicting the combined effects of various chemicals and their interactions with genetic backgrounds. iPSCs and iPSC-derived neuronal cells are known to often exhibit inconsistent behaviors and responses, due likely to their genetic variations.[146] Although the two NPC lines used in this study showed similar characteristics in their molecular profiles (Figures 1, 2, and S2), and were indistinguishable in the t-SNE plot based on calcium trace image data (Figure 5A), increasing statistical power may help reveal how a diverse population with different genetic background would differently respond to a substance of interest. While the use of NPCs offers various advantages, their immature electrophysiological and molecular characteristics do not fully inform us about the effects of chemicals on mature neurons. Therefore, testing additional NPCs and neurons derived from different donors would be crucial.

The lack of architectural transparency in Google AutoML Vision is computational limitation. While the AutoML Vision model provided superior precision, recall, and classification compared to several other machine learning algorithms in our intended application (Table S5) through automated hyperparameter tuning, it operates as a black-box system by design. This conceals essential architectural details such as the layer count, filter size, stride value, padding type, and activation function. The lack of transparency hinders the ability to gain insights into the decision-making process and to diagnose and correct problems and biases, affecting the interpretability and optimization of the model. Implementing post-processing techniques based on game theory[147,148] may help address the interpretability issue and allow the identification of features of the input dataset that play a leading role in prediction of chemical effects.

RESOURCE AVAILABILITY

Lead contact

Request for further information and resources should be directed to the lead contact Prof. Kazue Hashimoto-Torii (khtorii@childrensnational.org).

Materials availability

This study did not generate new materials.

Data and code availability

- RNA sequencing data used in this study are available at GEO under accession number GSE164499 and listed in the key resources table. This study also analyzes publicly available datasets, with references and URLs provided in the key resources table.
- Code used in this study is publicly available at https://github.com/BansalAnkush/Chemical-Effects-on-NPCs. The AutoML Vision models used in this study are available upon request from the lead contact.
- Any additional information required to reanalyze the data reported in this paper is available from the lead contact upon request.

ACKNOWLEDGMENTS

This work was supported by the NIH/NIAAA F32AA028163 (RYK), NIH/NIAAA R01AA026272 (MT and KHT), Scott-Gentle Foundation (MT and KHT), Suntory MONOZUKURI Expert Limited (KHT), and the District of Columbia Intellectual and Developmental Disabilities Research Center (DC-IDDRC) Award P50HD105328 by NICHD (PI: V. Gallo). We thank Dr. Nathan Smith for technical assistance with calcium imaging. We also thank Drs. Keiji Sugai and Amy Hwang for assisstance in data processing.

AUTHOR CONTRIBUTIONS

Conceptualization: K.H.-T. and M.T.; methodology: K.H.-T., T.U., R.Y.K., and A.B.; investigation: R.Y.K., A.B., and K.H.-T.; formal analysis: R.Y.K., A.B., D.V., J.P., and S.Y.; visualization: A.B. and R.Y.K.; supervision: K.H.-T. and M.T.; writing—original draft: R.Y.K., A.B., and D.J.D.; writing—review and editing: M.T. and K.H.-T.; funding acquisition: K.H.-T., M.T., and R.Y.K.

DECLARATION OF INTERESTS

K.H.-T. has received research funding from Suntory MONOZUKURI Expert Limited. T.U. is an employee of Suntory MONOZUKURI Expert Limited.

STAR★METHODS

Detailed methods are provided in the online version of this paper and include the following:

- KEY RESOURCES TABLE
- EXPERIMENTAL MODEL AND STUDY PARTICIPANT DETAILS
  - Culture of iPSC-derived NPCs
- METHOD DETAILS
  - Library preparation and bulk RNA-seq
  - Bulk RNA-seq data analysis
  - Single cell RNA-seq
  - Assessment of molecular profile similarity between NPC lines
  - Chemical treatment of NPCs
  - Calcium imaging
  - Immunocytochemistry
  - Conversion of calcium activity traces to image files for machine learning with AutoML vision
  - Feature extraction from calcium imaging data
  - t-distributed stochastic neighbor embedding (t-SNE) analysis
  - Neural Architecture Search (NAS)
  - AutoML vision model training
  - Assessment of the bioactivity and physiochemical properties of chemicals by ChemMine tools
- QUANTIFICATION AND STATISTICAL ANALYSIS
  - Statistical analysis of features in calcium dynamics
  - Performance metrics calculation
  - Safety score and similarity matrix calculation

SUPPLEMENTAL INFORMATION

Supplemental information can be found online at https://doi.org/10.1016/j.isci.2024.111298.

Received: June 8, 2023
Revised: July 24, 2024
Accepted: October 29, 2024
Published: November 1, 2024

REFERENCES

1. Curran, C.P., and Marczinski, C.A. (2017). Taurine, caffeine, and energy drinks: Reviewing the risks to the adolescent brain. Birth Defects Res. *109*, 1640–1648. https://doi.org/10.1002/bdr2.1177.

2. Harry, G.J., and Tiffany-Castiglioni, E. (2005). Evaluation of neurotoxic potential by use of *in vitro* systems. Expert Opin. Drug Metab. Toxicol. *1*, 701–713. https://doi.org/10.1517/17425255.1.4.701.

3. Accardi, M.V., Pugsley, M.K., Forster, R., Troncy, E., Huang, H., and Authier, S. (2016). The emerging role of *in vitro* electrophysiological methods in CNS safety pharmacology. J. Pharmacol. Toxicol. Methods *81*, 47–59. https://doi.org/10.1016/j.vascn.2016.03.008.

4. Farrell, K., Joshi, P., Roth, A., Kothapalli, C., and Lee, M.Y. (2016). High-throughput Screening of Toxic Chemicals on Neural Stem Cells. https://doi.org/10.1039/9781782626787-00031.

5. Matsuda, N., Odawara, A., Kinoshita, K., Okamura, A., Shirakawa, T., and Suzuki, I. (2022). Raster plots machine learning to predict the seizure liability of drugs and to identify drugs. Sci. Rep. *12*, 2281. https://doi.org/10.1038/s41598-022-05697-8.

6. Johnstone, A.F.M., Gross, G.W., Weiss, D.G., Schroeder, O.H.U., Gramowski, A., and Shafer, T.J. (2010). Microelectrode arrays: A physiologically based neurotoxicity testing platform for the 21st century. Neurotoxicology *31*, 331–350. https://doi.org/10.1016/j.neuro.2010.04.001.

7. Defranchi, E., Novellino, A., Whelan, M., Vogel, S., Ramirez, T., van Ravenzwaay, B., and Landsiedel, R. (2011). Feasibility Assessment of Micro-Electrode Chip Assay as a Method of Detecting Neurotoxicity *in vitro*. Front. Neuroeng. *4*, 6. https://doi.org/10.3389/fneng.2011.00006.

8. Buccino, A.P., Kordovan, M., Ness, T.V., Merkt, B., Häfliger, P.D., Fyhn, M., Cauwenberghs, G., Rotter, S., and Einevoll, G.T. (2018). Combining biophysical modeling and deep learning for multielectrode array neuron localization and classification. J. Neurophysiol. *120*, 1212–1232. https://doi.org/10.1152/jn.00210.2018.

9. Hornauer, P., Prack, G., Anastasi, N., Ronchi, S., Kim, T., Donner, C., Fiscella, M., Borgwardt, K., Taylor, V., Jagasia, R., et al. (2024). DeePhys: A machine learning–assisted platform for electrophysiological phenotyping of human neuronal networks. Stem Cell Rep. *19*, 285–298. https://doi.org/10.1016/j.stemcr.2023.12.008.

10. Weir, K., Blanquie, O., Kilb, W., Luhmann, H.J., and Sinning, A. (2014). Comparison of spike parameters from optically identified GABAergic and glutamatergic neurons in sparse cortical cultures. Front. Cell. Neurosci. *8*, 460. https://doi.org/10.3389/fncel.2014.00460.

11. Blankenship, A.G., and Feller, M.B. (2010). Mechanisms underlying spontaneous patterned activity in developing neural circuits. Nat. Rev. Neurosci. *11*, 18–29. https://doi.org/10.1038/nrn2759.

12. Rosenberg, S.S., and Spitzer, N.C. (2011). Calcium signaling in neuronal development. Cold Spring Harb. Perspect. Biol. *3*, a004259. https://doi.org/10.1101/cshperspect.a004259.

13. Higley, M.J., and Sabatini, B.L. (2012). Calcium signaling in dendritic spines. Cold Spring Harb. Perspect. Biol. *4*, a005686. https://doi.org/10.1101/cshperspect.a005686.

14. Berridge, M.J., Lipp, P., and Bootman, M.D. (2000). The versatility and universality of calcium signalling. Nat. Rev. Mol. Cell Biol. *1*, 11–21. https://doi.org/10.1038/35036035.

15. Kim, J.W., Oh, H.A., Lee, S.H., Kim, K.C., Eun, P.H., Ko, M.J., Gonzales, E.L.T., Seung, H., Kim, S., Bahn, G.H., and Shin, C.Y. (2018). T-Type Calcium Channels Are Required to Maintain Viability of Neural Progenitor Cells. Biomol. Ther. *26*, 439–445. https://doi.org/10.4062/biomolther.2017.223.

16. Weissman, T.A., Riquelme, P.A., Ivic, L., Flint, A.C., and Kriegstein, A.R. (2004). Calcium waves propagate through radial glial cells and modulate proliferation in the developing neocortex. Neuron *43*, 647–661. https://doi.org/10.1016/j.neuron.2004.08.015.

17. Lohmann, C., and Bonhoeffer, T. (2008). A role for local calcium signaling in rapid synaptic partner selection by dendritic filopodia. Neuron *59*, 253–260. https://doi.org/10.1016/j.neuron.2008.05.025.

18. Pnevmatikakis, E.A., Soudry, D., Gao, Y., Machado, T.A., Merel, J., Pfau, D., Reardon, T., Mu, Y., Lacefield, C., Yang, W., et al. (2016). Simultaneous Denoising, Deconvolution, and Demixing of Calcium Imaging Data. Neuron *89*, 285–299. https://doi.org/10.1016/j.neuron.2015.11.037.

19. Giovannucci, A., Friedrich, J., Gunn, P., Kalfon, J., Brown, B.L., Koay, S.A., Taxidis, J., Najafi, F., Gauthier, J.L., Zhou, P., et al. (2019). CaImAn an open source tool for scalable calcium imaging data analysis. Elife *8*, e38173. https://doi.org/10.7554/eLife.38173.

20. Dursun, G., Bijelić, D., Ayşit, N., Kurt Vatandaşlar, B., Radenović, L., Çapar, A., Kerman, B.E., Andjus, P.R., Korenić, A., and Özkaya, U. (2023). Combined segmentation and classification-based approach to automated analysis of biomedical signals obtained from calcium imaging. PLoS One *18*, e0281236. https://doi.org/10.1371/journal.pone.0281236.

21. This, S., Costantino, S., and Melichar, H.J. (2024). Machine learning predictions of T cell antigen specificity from intracellular calcium dynamics. Sci. Adv. *10*, eadk2298. https://doi.org/10.1126/sciadv.adk2298.

22. Chen, Y., and Huang, L.Y.M. (2017). A simple and fast method to image calcium activity of neurons from intact dorsal root ganglia using fluorescent chemical Ca2+ indicators. Mol. Pain *13*, 1744806917748051. https://doi.org/10.1177/1744806917748051.

23. Palazzolo, G., Moroni, M., Soloperto, A., Aletti, G., Naldi, G., Vassalli, M., Nieus, T., and Difato, F. (2017). Fast wide-volume functional imaging of engineered *in vitro* brain tissues. Sci. Rep. *7*, 8499. https://doi.org/10.1038/s41598-017-08979-8.

24. Wu, N., Nishioka, W.K., Derecki, N.C., and Maher, M.P. (2019). High-throughput-compatible assays using a genetically-encoded calcium indicator. Sci. Rep. *9*, 12692. https://doi.org/10.1038/s41598-019-49070-8.

25. Kowalczewski, A., Sakolish, C., Hoang, P., Liu, X., Jacquir, S., Rusyn, I., and Ma, Z. (2022). Integrating nonlinear analysis and machine learning for human induced pluripotent stem cell-based drug cardiotoxicity testing. J. Tissue Eng. Regen. Med. *16*, 732–743. https://doi.org/10.1002/term.3325.

26. Sirenko, O., Parham, F., Dea, S., Sodhi, N., Biesmans, S., Mora-Castilla, S., Ryan, K., Behl, M., Chandy, G., Crittenden, C., et al. (2019). Functional and Mechanistic Neurotoxicity Profiling Using Human iPSC-Derived Neural 3D Cultures. Toxicol. Sci. *167*, 58–76. https://doi.org/10.1093/toxsci/kfy218.

27. Walter, J., and Dihné, M. (2012). Species-dependent differences of embryonic stem cell-derived neural stem cells after Interferon gamma treatment. Front. Cell. Neurosci. *6*, 52. https://doi.org/10.3389/fncel.2012.00052.

28. D'Aiuto, L., Zhi, Y., Kumar Das, D., Wilcox, M.R., Johnson, J.W., McClain, L., MacDonald, M.L., Di Maio, R., Schurdak, M.E., Piazza, P., et al. (2014). Large-scale generation of human iPSC-derived neural stem cells/early neural progenitor cells and their neuronal differentiation. Organogenesis *10*, 365–377. https://doi.org/10.1080/15476278.2015.1011921.

29. McLaren, D., Gorba, T., Marguerie de Rotrou, A., Pillai, G., Chappell, C., Stacey, A., Lingard, S., Falk, A., Smith, A., Koch, P., et al. (2013). Automated large-scale culture and medium-throughput chemical screen for modulators of proliferation and viability of human induced pluripotent stem cell-derived neuroepithelial-like stem cells. J. Biomol. Screen *18*, 258–268. https://doi.org/10.1177/1087057112461446.

30. Hulme, A.J., Maksour, S., St-Clair Glover, M., Miellet, S., and Dottori, M. (2021). Making neurons, made easy: The use of Neurogenin-2 in neuronal differentiation. Stem Cell Rep. *17*, 14–34. https://doi.org/10.1016/j.stemcr.2021.11.015.

31. Prè, D., Nestor, M.W., Sproul, A.A., Jacob, S., Koppensteiner, P., Chinchalongporn, V., Zimmer, M., Yamamoto, A., N oggle, S.A., and Arancio, O. (2014). A time course analysis of the electrophysiological properties of neurons differentiated from human induced pluripotent stem cells (iPSCs). PLoS One *9*, e103418. https://doi.org/10.1371/journal.pone.0103418.

32. Rosa, F., Dhingra, A., Uysal, B., Mendis, G.D.C., Loeffler, H., Elsen, G., Mueller, S., Schwarz, N., Castillo-Lizardo, M., Cuddy, C., et al. (2020). In Vitro Differentiated Human Stem Cell-Derived Neurons Reproduce

Synaptic Synchronicity Arising during Neurodevelopment. Stem Cell Rep. *15*, 22–37. https://doi.org/10.1016/j.stemcr.2020.05.015.

33. Lin, H.C., He, Z., Ebert, S., Schörnig, M., Santel, M., Nikolova, M.T., Weigert, A., Hevers, W., Kasri, N.N., Taverna, E., et al. (2021). NGN2 induces diverse neuron types from human pluripotency. Stem Cell Rep. *16*, 2118–2127. https://doi.org/10.1016/j.stemcr.2021.07.006.
34. Lam, M., Sanosaka, T., Lundin, A., Imaizumi, K., Etal, D., Karlsson, F.H., Clausen, M., Cairns, J., Hicks, R., Kohyama, J., et al. (2019). Single-cell study of neural stem cells derived from human iPSCs reveals distinct progenitor populations with neurogenic and gliogenic potential. Gene Cell. *24*, 836–847. https://doi.org/10.1111/gtc.12731.
35. Fantuzzo, J.A., Robles, D.A., Mirabella, V.R., Hart, R.P., Pang, Z.P., and Zahn, J.D. (2020). Development of a high-throughput arrayed neural circuitry platform using human induced neurons for drug screening applications. Lab Chip *20*, 1140–1152. https://doi.org/10.1039/c9lc01179j.
36. Lu, H.R., Seo, M., Kreir, M., Tanaka, T., Yamoto, R., Altrocchi, C., van Ammel, K., Tekle, F., Pham, L., Yao, X., et al. (2023). High-Throughput Screening Assay for Detecting Drug-Induced Changes in Synchronized Neuronal Oscillations and Potential Seizure Risk Based on Ca(2+) Fluorescence Measurements in Human Induced Pluripotent Stem Cell (hiPSC)-Derived Neuronal 2D and 3D Cultures. Cells *12*, 958. https://doi.org/10.3390/cells12060958.
37. Boivin, B., Roet, K.C.D., Huang, X., Karhohs, K.W., Rohban, M.H., Sandoe, J., Wiskow, O., Maeda, R., Grantham, A., Dornon, M.K., et al. (2022). A multiparametric activity profiling platform for neuron disease phenotyping and drug screening. Mol. Biol. Cell *33*, ar54. https://doi.org/10.1091/mbc.E21-10-0481.
38. Li, T., Jiang, L., Chen, H., and Zhang, X. (2008). Characterization of excitability and voltage-gated ion channels of neural progenitor cells in rat hippocampus. J. Mol. Neurosci. *35*, 289–295. https://doi.org/10.1007/s12031-008-9065-7.
39. Young, A., Machacek, D.W., Dhara, S.K., Macleish, P.R., Benveniste, M., Dodla, M.C., Sturkie, C.D., and Stice, S.L. (2011). Ion channels and ionotropic receptors in human embryonic stem cell derived neural progenitors. Neuroscience *192*, 793–805. https://doi.org/10.1016/j.neuroscience.2011.04.039.
40. Lorenz, C., Lesimple, P., Bukowiecki, R., Zink, A., Inak, G., Mlody, B., Singh, M., Semtner, M., Mah, N., Auré, K., et al. (2017). Human iPSC-Derived Neural Progenitors Are an Effective Drug Discovery Model for Neurological mtDNA Disorders. Cell Stem Cell *20*, 659–674.e9. https://doi.org/10.1016/j.stem.2016.12.013.
41. Vőfély, G., Berecz, T., Szabó, E., Szebényi, K., Hathy, E., Orbán, T.I., Sarkadi, B., Homolya, L., Marchetto, M.C., Réthelyi, J.M., et al. (2018). Characterization of calcium signals in human induced pluripotent stem cell-derived dentate gyrus neuronal progenitors and mature neurons, stably expressing an advanced calcium indicator protein. Mol. Cell. Neurosci. *88*, 222–240. https://doi.org/10.1016/j.mcn.2018.02.003.
42. Readhead, B., Hartley, B.J., Eastwood, B.J., Collier, D.A., Evans, D., Farias, R., He, C., Hoffman, G., Sklar, P., Dudley, J.T., et al. (2018). Expression-based drug screening of neural progenitor cells from individuals with schizophrenia. Nat. Commun. *9*, 4412. https://doi.org/10.1038/s41467-018-06515-4.
43. Walter, J., Bolognin, S., Antony, P.M.A., Nickels, S.L., Poovathingal, S.K., Salamanca, L., Magni, S., Perfeito, R., Hoel, F., Qing, X., et al. (2019). Neural Stem Cells of Parkinson's Disease Patients Exhibit Aberrant Mitochondrial Morphology and Functionality. Stem Cell Rep. *12*, 878–889. https://doi.org/10.1016/j.stemcr.2019.03.004.
44. de Groot, M.W.G.D.M., Dingemans, M.M.L., Rus, K.H., de Groot, A., and Westerink, R.H.S. (2014). Characterization of calcium responses and electrical activity in differentiating mouse neural progenitor cells *in vitro*. Toxicol. Sci. *137*, 428–435. https://doi.org/10.1093/toxsci/kft261.
45. Tran, T.T.V., Surya Wibowo, A., Tayara, H., and Chong, K.T. (2023). Artificial Intelligence in Drug Toxicity Prediction: Recent Advances, Challenges, and Future Perspectives. J. Chem. Inf. Model. *63*, 2628–2643. https://doi.org/10.1021/acs.jcim.3c00200.
46. Mayr, A., Klambauer, G., Unterthiner, T., and Hochreiter, S. (2016). DeepTox: Toxicity Prediction using Deep Learning. Front. Environ. Sci. *3*, 80.
47. Hao, Y., Romano, J.D., and Moore, J.H. (2022). Knowledge-guided deep learning models of drug toxicity improve interpretation. Patterns *3*, 100565.
48. Li, T., Liu, Z., Thakkar, S., Roberts, R., and Tong, W. (2023). DeepAmes: A deep learning-powered Ames test predictive model with potential for regulatory application. Regul. Toxicol. Pharmacol. *144*, 105486. https://doi.org/10.1016/j.yrtph.2023.105486.
49. Wilm, A., Stork, C., Bauer, C., Schepky, A., Kühnl, J., and Kirchmair, J. (2019). Skin Doctor: Machine Learning Models for Skin Sensitization Prediction that Provide Estimates and Indicators of Prediction Reliability. Int. J. Mol. Sci. *20*, 4833. https://doi.org/10.3390/ijms20194833.
50. Pu, L., Naderi, M., Liu, T., Wu, H.C., Mukhopadhyay, S., and Brylinski, M. (2019). eToxPred: a machine learning-based approach to estimate the toxicity of drug candidates. BMC Pharmacol. Toxicol. *20*, 2. https://doi.org/10.1186/s40360-018-0282-6.
51. Adeluwa, T., McGregor, B.A., Guo, K., and Hur, J. (2021). Predicting Drug-Induced Liver Injury Using Machine Learning on a Diverse Set of Predictors. Front. Pharmacol. *12*, 648805. https://doi.org/10.3389/fphar.2021.648805.
52. Jamal, S., Ali, W., Nagpal, P., Grover, S., and Grover, A. (2019). Computational models for the prediction of adverse cardiovascular drug reactions. J. Transl. Med. *17*, 171. https://doi.org/10.1186/s12967-019-1918-z.
53. Zhu, Q., Song, L., Peng, G., Sun, N., Chen, J., Zhang, T., Sheng, N., Tang, W., Qian, C., Qiao, Y., et al. (2014). The transcription factor Pou3f1 promotes neural fate commitment via activation of neural lineage genes and inhibition of external signaling pathways. Elife *3*, e02224. https://doi.org/10.7554/eLife.02224.
54. Brennand, K., Savas, J.N., Kim, Y., Tran, N., Simone, A., Hashimoto-Torii, K., Beaumont, K.G., Kim, H.J., Topol, A., Ladran, I., et al. (2015). Phenotypic differences in hiPSC NPCs derived from patients with schizophrenia. Mol. Psychiatry *20*, 361–368. https://doi.org/10.1038/mp.2014.22.
55. LoTurco, J.J., Owens, D.F., Heath, M.J., Davis, M.B., and Kriegstein, A.R. (1995). GABA and glutamate depolarize cortical progenitor cells and inhibit DNA synthesis. Neuron *15*, 1287–1298. https://doi.org/10.1016/0896-6273(95)90008-x.
56. Petrik, D., Myoga, M.H., Grade, S., Gerkau, N.J., Pusch, M., Rose, C.R., Grothe, B., and Götz, M. (2018). Epithelial Sodium Channel Regulates Adult Neural Stem Cell Proliferation in a Flow-Dependent Manner. Cell Stem Cell *22*, 865–878.e8. https://doi.org/10.1016/j.stem.2018.04.016.
57. Schaarschmidt, G., Wegner, F., Schwarz, S.C., Schmidt, H., and Schwarz, J. (2009). Characterization of voltage-gated potassium channels in human neural progenitor cells. PLoS One *4*, e6168. https://doi.org/10.1371/journal.pone.0006168.
58. Andhika Rhaditya, P.A., Oishi, K., Nishimura, Y.V., and Motoyama, J. (2022). [Ca(2+)](i) fluctuation mediated by T-type Ca(2+) channel is required for the differentiation of cortical neural progenitor cells. Dev. Biol. *489*, 84–97. https://doi.org/10.1016/j.ydbio.2022.05.021.
59. Ferrer, I., Garcia-Esparcia, P., Carmona, M., Carro, E., Aronica, E., Kovacs, G.G., Grison, A., and Gustincich, S. (2016). Olfactory Receptors in Non-Chemosensory Organs: The Nervous System in Health and Disease. Front. Aging Neurosci. *8*, 163. https://doi.org/10.3389/fnagi.2016.00163.
60. Kurvits, K., Laius, O., Uusküla, M., Haldre, S., and Rakitin, A. (2020). Valproic acid prescription trends among females of childbearing age in Estonia: A 14-year nationwide prescription database study. Seizure *76*, 28–31. https://doi.org/10.1016/j.seizure.2020.01.004.

61. Eckert, M., Klumpp, L., and Huber, S.M. (2017). Cellular Effects of the Antiepileptic Drug Valproic Acid in Glioblastoma. Cell. Physiol. Biochem. *44*, 1591–1605. https://doi.org/10.1159/000485753.

62. Mitchell, D.C., Knight, C.A., Hockenberry, J., Teplansky, R., and Hartman, T.J. (2014). Beverage caffeine intakes in the U.S. Food Chem. Toxicol. *63*, 136–142. https://doi.org/10.1016/j.fct.2013.10.042.

63. National Institute on Alcohol Abuse and Alcoholism (2021). Understanding the Dangers of Alcohol Overdose.

64. Richards, D.G., McPherson, J.J., Evans, K.T., and Rosen, M. (1986). Effect of volume of water taken with diazepam tablets on absorption. Br. J. Anaesth. *58*, 41–44. https://doi.org/10.1093/bja/58.1.41.

65. McPherson, P.S., Kim, Y.K., Valdivia, H., Knudson, C.M., Takekura, H., Franzini-Armstrong, C., Coronado, R., and Campbell, K.P. (1991). The brain ryanodine receptor: a caffeine-sensitive calcium release channel. Neuron *7*, 17–25. https://doi.org/10.1016/0896-6273(91)90070-g.

66. Vernikos-Danellis, J., and Harris, C.G. (1968). The Effect of in Vitro and in Vivo Caffeine, Theophylline, and Hydrocortisone on the Phosphodiesterase Activity of the Pituitary, Median Eminence, Heart, and Cerebral Cortex of the Rat. Exp. Biol. Med. (Maywood). *128*, 1016–1021. https://doi.org/10.3181/00379727-128-33183.

67. Chen, Y., Xiao, P., Ou-Yang, D.S., Fan, L., Guo, D., Wang, Y.N., Han, Y., Tu, J.H., Zhou, G., Huang, Y.F., and Zhou, H.H. (2009). Simultaneous action of the flavonoid quercetin on cytochrome P450 (CYP) 1A2, CYP2A6, N-acetyltransferase and xanthine oxidase activity in healthy volunteers. Clin. Exp. Pharmacol. Physiol. *36*, 828–833. https://doi.org/10.1111/j.1440-1681.2009.05158.x.

68. EFSA Panel on Dietetic Products, Nutrition and Allergies (NDA) (2015). Scientific Opinion on the safety of caffeine. EFSA J. *13*, 4102. https://doi.org/10.2903/j.efsa.2015.4102.

69. Rha, J.H., Jang, I.J., Lee, K.H., Chong, W.S., Shin, S.G., Lee, N., and Myung, H.J. (1993). Pharmacokinetic comparison of two valproic acid formulations–a plain and a controlled release enteric-coated tablets. J. Korean Med. Sci. *8*, 251–256. https://doi.org/10.3346/jkms.1993.8.4.251.

70. Barile, F.A., Dierickx, P.J., and Kristen, U. (1994). In vitro cytotoxicity testing for prediction of acute human toxicity. Cell Biol. Toxicol. *10*, 155–162. https://doi.org/10.1007/BF00757558.

71. Hengstler, J.G., Sjögren, A.K., Zink, D., and Hornberg, J.J. (2020). In vitro prediction of organ toxicity: the challenges of scaling and secondary mechanisms of toxicity. Arch. Toxicol. *94*, 353–356. https://doi.org/10.1007/s00204-020-02669-7.

72. Woodward, J.J., and Pava, M. (2012). Ethanol inhibition of up-states in prefrontal cortical neurons expressing the genetically encoded calcium indicator GCaMP3. Alcohol Clin. Exp. Res. *36*, 780–787. https://doi.org/10.1111/j.1530-0277.2011.01674.x.

73. Cunningham, M.L. (1965). Acute hepatic necrosis following treatment with amitriptyline and diazepam. Br. J. Psychiatry *111*, 1107–1109. https://doi.org/10.1192/bjp.111.480.1107.

74. Jones, A.W., and Holmgren, A. (2013). Concentrations of diazepam and nordiazepam in 1,000 blood samples from apprehended drivers–therapeutic use or abuse of anxiolytics? J. Pharm. Pract. *26*, 198–203. https://doi.org/10.1177/0897190012451910.

75. Spiller, H.A., Krenzelok, E.P., Klein-Schwartz, W., Winter, M.L., Weber, J.A., Sollee, D.R., Bangh, S.A., and Griffith, J.R. (2000). Multicenter case series of valproic acid ingestion: serum concentrations and toxicity. J. Toxicol. Clin. Toxicol. *38*, 755–760. https://doi.org/10.1081/clt-100102388.

76. Ikeda, H., Delargy, A.H., Yokogawa, T., Urban, J.M., Burgess, H.A., and Ono, F. (2013). Intrinsic properties of larval zebrafish neurons in ethanol. PLoS One *8*, e63318. https://doi.org/10.1371/journal.pone.0063318.

77. Nehlig, A., Daval, J.L., and Debry, G. (1992). Caffeine and the central nervous system: mechanisms of action, biochemical, metabolic and psychostimulant effects. Brain research. Brain Res. Rev. *17*, 139–170. https://doi.org/10.1016/0165-0173(92)90012-b.

78. Parys, J.B., Bootman, M.D., Yule, D.I., and Bultynck, G. (2014). Calcium Techniques: A Laboratory Manual (Cold Spring Harbor Laboratory Press).

79. Overk, C.R., Rockenstein, E., Florio, J., Cheng, Q., and Masliah, E. (2015). Differential calcium alterations in animal models of neurodegenerative disease: Reversal by FK506. Neuroscience *310*, 549–560. https://doi.org/10.1016/j.neuroscience.2015.08.068.

80. Brockhaus, J., Brüggen, B., and Missler, M. (2019). Imaging and Analysis of Presynaptic Calcium Influx in Cultured Neurons Using synGCaMP6f. Front. Synaptic Neurosci. *11*, 12. https://doi.org/10.3389/fnsyn.2019.00012.

81. Salgado-Almario, J., Vicente, M., Vincent, P., Domingo, B., and Llopis, J. (2020). Mapping Calcium Dynamics in the Heart of Zebrafish Embryos with Ratiometric Genetically Encoded Calcium Indicators. Int. J. Mol. Sci. *21*, 6610. https://doi.org/10.3390/ijms21186610.

82. Semyanov, A., Henneberger, C., and Agarwal, A. (2020). Making sense of astrocytic calcium signals - from acquisition to interpretation. Nat. Rev. Neurosci. *21*, 551–564. https://doi.org/10.1038/s41583-020-0361-8.

83. Romano, S.A., Pérez-Schuster, V., Jouary, A., Boulanger-Weill, J., Candeo, A., Pietri, T., and Sumbre, G. (2017). An integrated calcium imaging processing toolbox for the analysis of neuronal population dynamics. PLoS Comput. Biol. *13*, e1005526. https://doi.org/10.1371/journal.pcbi.1005526.

84. Zoph, B., Vasudevan, V., Shlens, J., and Le, Q.V. (2018). Learning Transferable Architectures for Scalable Image Recognition, pp. 8697–8710.

85. Breiman, L. (2001). Random Forests. Mach. Learn. *45*, 5–32. https://doi.org/10.1023/A:1010933404324.

86. Liaw, A., and Wiener, M. (2001). Classification and Regression by RandomForest. Forest *23*, 18–22.

87. Fernández-Delgado, M., Cernadas, E., Barro, S., and Amorim, D. (2014). Do we Need Hundreds of Classifiers to Solve Real World Classification Problems? J. Mach. Learn. Res. *15*, 3133–3181.

88. Biau, G., and Scornet, E. (2016). A random forest guided tour. Test *25*, 197–227. https://doi.org/10.1007/s11749-016-0481-7.

89. Elith, J., Leathwick, J.R., and Hastie, T. (2008). A working guide to boosted regression trees. J. Anim. Ecol. *77*, 802–813. https://doi.org/10.1111/j.1365-2656.2008.01390.x.

90. Friedman, J.H. (2001). Greedy Function Approximation: A Gradient Boosting Machine. Ann. Statist. *29*, 1189–1232. https://doi.org/10.1214/aos/1013203451.

91. Natekin, A., and Knoll, A. (2013). Gradient boosting machines, a tutorial. Front. Neurorobot. *7*, 21. https://doi.org/10.3389/fnbot.2013.00021.

92. LeCun, Y., Bengio, Y., and Hinton, G. (2015). Deep learning. Nature *521*, 436–444. https://doi.org/10.1038/nature14539.

93. Shen, D., Wu, G., and Suk, H.I. (2017). Deep Learning in Medical Image Analysis. Annu. Rev. Biomed. Eng. *19*, 221–248. https://doi.org/10.1146/annurev-bioeng-071516-044442.

94. Litjens, G., Kooi, T., Bejnordi, B.E., Setio, A.A.A., Ciompi, F., Ghafoorian, M., van der Laak, J.A.W.M., van Ginneken, B., and Sánchez, C.I. (2017). A survey on deep learning in medical image analysis. Med. Image Anal. *42*, 60–88. https://doi.org/10.1016/j.media.2017.07.005.

95. Cristianini, N., and Shawe-Taylor, J. (2000). An Introduction to Support Vector Machines and Other Kernel-Based Learning Methods (Cambridge University Press). https://doi.org/10.1017/CBO9780511801389.

96. Boser, B.E., Guyon, I.M., and Vapnik, V.N. (1992). A Training Algorithm for Optimal Margin Classifiers (Association for Computing Machinery), pp. 144–152.

97. Schölkopf, B., Platt, J.C., Shawe-Taylor, J., Smola, A.J., and Williamson, R.C. (2001). Estimating the support of a high-dimensional distribution.

Neural Comput. *13*, 1443–1471. https://doi.org/10.1162/089976601750264965.

98. Kuhn, M., and Johnson, K. (2013). Applied Predictive Modeling (Springer). https://doi.org/10.1007/978-1-4614-6849-3.
99. Esteva, A., Kuprel, B., Novoa, R.A., Ko, J., Swetter, S.M., Blau, H.M., and Thrun, S. (2017). Dermatologist-level classification of skin cancer with deep neural networks. Nature *542*, 115–118. https://doi.org/10.1038/nature21056.
100. Adinoff, B., Bone, G.H., and Linnoila, M. (1988). Acute ethanol poisoning and the ethanol withdrawal syndrome. Med. Toxicol. Adverse Drug Exp. *3*, 172–196. https://doi.org/10.1007/bf03259881.
101. Cappelletti, S., Piacentino, D., Fineschi, V., Frati, P., Cipolloni, L., and Aromatario, M. (2018). Caffeine-Related Deaths: Manner of Deaths and Categories at Risk. Nutrients *10*, 611. https://doi.org/10.3390/nu10050611.
102. Chen, W.B., Gao, R., Su, Y.Y., Zhao, J.W., Zhang, Y.Z., Wang, L., Ren, Y., and Fan, C.Q. (2011). Valproate versus diazepam for generalized convulsive status epilepticus: a pilot study. Eur. J. Neurol. *18*, 1391–1396. https://doi.org/10.1111/j.1468-1331.2011.03420.x.
103. Rasch, V. (2003). Cigarette, alcohol, and caffeine consumption: risk factors for spontaneous abortion. Acta Obstet. Gynecol. Scand. *82*, 182–188. https://doi.org/10.1034/j.1600-0412.2003.00078.x.
104. Owens, D.C. (2019). Sodium valproate in psychiatric practice: time for a change in perception. Br. J. Psychiatry *215*, 516–518. https://doi.org/10.1192/bjp.2019.137.
105. Backman, T.W.H., Cao, Y., and Girke, T. (2011). ChemMine tools: an online service for analyzing and clustering small molecules. Nucleic Acids Res. *39*, W486–W491. https://doi.org/10.1093/nar/gkr320.
106. Deng, P., Ma, Q., Xi, Y., Yang, L., Lin, M., Yu, Z., Chen, C., and Zhou, Z. (2020). Transcriptomic insight into cadmium-induced neurotoxicity in embryonic neural stem/progenitor cells. Toxicol. Vitro *62*, 104686. https://doi.org/10.1016/j.tiv.2019.104686.
107. Mahajan, G., Lee, M.Y., and Kothapalli, C. (2019). Biophysical and biomechanical properties of neural progenitor cells as indicators of developmental neurotoxicity. Arch. Toxicol. *93*, 2979–2992. https://doi.org/10.1007/s00204-019-02549-9.
108. Reichert, K.P., Schetinger, M.R.C., Pillat, M.M., Bottari, N.B., Palma, T.V., Gutierres, J.M., Ulrich, H., Andrade, C.M., Exley, C., and Morsch, V.M.M. (2019). Aluminum affects neural phenotype determination of embryonic neural progenitor cells. Arch. Toxicol. *93*, 2515–2524. https://doi.org/10.1007/s00204-019-02522-6.
109. Yoneyama, M., Seko, K., Kawada, K., Sugiyama, C., and Ogita, K. (2009). High susceptibility of cortical neural progenitor cells to trimethyltin toxicity: involvement of both caspases and calpain in cell death. Neurochem. Int. *55*, 257–264. https://doi.org/10.1016/j.neuint.2009.03.008.
110. Cui, J., Liu, Y., Chang, X., Gou, W., Zhou, X., Liu, Z., Li, Z., Wu, Y., and Zuo, D. (2019). Acetaldehyde Induces Neurotoxicity In Vitro via Oxidative Stress- and Ca(2+) Imbalance-Mediated Endoplasmic Reticulum Stress T2. Oxid. Med. Cell. Longev. *2019*, 2593742. https://doi.org/10.1155/2019/2593742.
111. Lundquist, F., Tygstrup, N., Winkler, K., Mellemgaard, K., and Munck-Petersen, S. (1962). Ethanol metabolism and production of free acetate in the human liver. J. Clin. Invest. *41*, 955–961. https://doi.org/10.1172/jci104574.
112. Usachev, Y., Shmigol, A., Pronchuk, N., Kostyuk, P., and Verkhratsky, A. (1993). Caffeine-induced calcium release from internal stores in cultured rat sensory neurons. Neuroscience *57*, 845–859. https://doi.org/10.1016/0306-4522(93)90029-f.
113. Ferreira, D.D.P., Stutz, B., de Mello, F.G., Reis, R.A.M., and Kubrusly, R.C.C. (2014). Caffeine potentiates the release of GABA mediated by NMDA receptor activation: Involvement of A1 adenosine receptors. Neuroscience *281*, 208–215. https://doi.org/10.1016/j.neuroscience.2014.09.060.
114. Pereira-Figueiredo, D., Brito, R., Araújo, D.S.M., Nascimento, A.A., Lyra, E.S.B., Cheibub, A.M.S.S., Pereira Netto, A.D., Ventura, A.L.M., Paes-de-Carvalho, R., and Calaza, K.C. (2020). Caffeine exposure ameliorates acute ischemic cell death in avian developing retina. Purinergic Signal. *16*, 41–59. https://doi.org/10.1007/s11302-020-09687-1.
115. Griessner, J., Pasieka, M., Böhm, V., Grössl, F., Kaczanowska, J., Pliota, P., Kargl, D., Werner, B., Kaouane, N., Strobelt, S., et al. (2021). Central amygdala circuit dynamics underlying the benzodiazepine anxiolytic effect. Mol. Psychiatry *26*, 534–544. https://doi.org/10.1038/s41380-018-0310-3.
116. Hong, S.J., Damron, D.S., and Murray, P.A. (1998). Benzodiazepines differentially inhibit phenylephrine-induced calcium oscillations in pulmonary artery smooth muscle cells. Anesthesiology *88*, 792–799. https://doi.org/10.1097/00000542-199803000-00032.
117. Sequerra, E.B., Goyal, R., Castro, P.A., Levin, J.B., and Borodinsky, L.N. (2018). NMDA Receptor Signaling Is Important for Neural Tube Formation and for Preventing Antiepileptic Drug-Induced Neural Tube Defects. J. Neurosci. *38*, 4762–4773. https://doi.org/10.1523/jneurosci.2634-17.2018.
118. Chen, M., Suzuki, A., Thakkar, S., Yu, K., Hu, C., and Tong, W. (2016). DILIrank: the largest reference drug list ranked by the risk for developing drug-induced liver injury in humans. Drug Discov. Today *21*, 648–653. https://doi.org/10.1016/j.drudis.2016.02.015.
119. Elmazar, M.M., and Nau, H. (1995). Ethanol potentiates valproic acid-induced neural tube defects (NTDs) in mice due to toxicokinetic interactions. Reprod. Toxicol. *9*, 427–433. https://doi.org/10.1016/0890-6238(95)00023-4.
120. Golmohammadi, R., Pejhan, A., Azhdari-Zarmehri, H., and Mohammad-Zadeh, M. (2013). The role of ethanol on the anticonvulsant effect of valproic acid and cortical microvascular changes after epileptogenesis in mice. Neurol. Sci. *34*, 1125–1131. https://doi.org/10.1007/s10072-012-1190-y.
121. Li, Y., Zhou, Y., Peng, L., and Zhao, Y. (2017). Reduced protein expressions of cytomembrane GABA(A)Rβ3 at different postnatal developmental stages of rats exposed prenatally to valproic acid. Brain Res. *1671*, 33–42. https://doi.org/10.1016/j.brainres.2017.06.018.
122. Briley, M.S., and Langer, S.Z. (1978). Influence of GABA receptor agonists and antagonists on the binding of 3H-diazepam to the benzodiazepine receptor. Eur. J. Pharmacol. *52*, 129–132. https://doi.org/10.1016/0014-2999(78)90031-6.
123. Mohler, H., and Okada, T. (1977). GABA receptor binding with 3H (+) bicuculline-methiodide in rat CNS. Nature *267*, 65–67. https://doi.org/10.1038/267065a0.
124. Richter, L., de Graaf, C., Sieghart, W., Varagic, Z., Mörzinger, M., de Esch, I.J.P., Ecker, G.F., and Ernst, M. (2012). Diazepam-bound GABAA receptor models identify new benzodiazepine binding-site ligands. Nat. Chem. Biol. *8*, 455–464. https://doi.org/10.1038/nchembio.917.
125. Squires, R.F., and Brastrup, C. (1977). Benzodiazepine receptors in rat brain. Nature *266*, 732–734. https://doi.org/10.1038/266732a0.
126. Mascia, M.P., Trudell, J.R., and Harris, R.A. (2000). Specific binding sites for alcohols and anesthetics on ligand-gated ion channels. Proc. Natl. Acad. Sci. USA *97*, 9305–9310. https://doi.org/10.1073/pnas.160128797.
127. Ariwodola, O.J., and Weiner, J.L. (2004). Ethanol potentiation of GABAergic synaptic transmission may be self-limiting: role of presynaptic GABA(B) receptors. J. Neurosci. *24*, 10679–10686. https://doi.org/10.1523/jneurosci.1768-04.2004.
128. Zhu, P.J., and Lovinger, D.M. (2006). Ethanol potentiates GABAergic synaptic transmission in a postsynaptic neuron/synaptic bouton preparation from basolateral amygdala. J. Neurophysiol. *96*, 433–441. https://doi.org/10.1152/jn.01380.2005.

129. Roberto, M., Madamba, S.G., Moore, S.D., Tallent, M.K., and Siggins, G.R. (2003). Ethanol increases GABAergic transmission at both pre- and postsynaptic sites in rat central amygdala neurons. Proc. Natl. Acad. Sci. USA *100*, 2053–2058. https://doi.org/10.1073/pnas.0437926100.

130. Sanna, E., Talani, G., Busonero, F., Pisu, M.G., Purdy, R.H., Serra, M., and Biggio, G. (2004). Brain steroidogenesis mediates ethanol modulation of GABAA receptor activity in rat hippocampus. J. Neurosci. *24*, 6521–6530. https://doi.org/10.1523/jneurosci.0075-04.2004.

131. Wan, F.J., Berton, F., Madamba, S.G., Francesconi, W., and Siggins, G.R. (1996). Low ethanol concentrations enhance GABAergic inhibitory postsynaptic potentials in hippocampal pyramidal neurons only after block of GABAB receptors. Proc. Natl. Acad. Sci. USA *93*, 5049–5054. https://doi.org/10.1073/pnas.93.10.5049.

132. Nie, Z., Schweitzer, P., Roberts, A.J., Madamba, S.G., Moore, S.D., and Siggins, G.R. (2004). Ethanol augments GABAergic transmission in the central amygdala via CRF1 receptors. Science (New York, N.Y.) *303*, 1512–1514. https://doi.org/10.1126/science.1092550.

133. Isokawa, M. (2016). Caffeine-Induced Suppression of GABAergic Inhibition and Calcium-Independent Metaplasticity. Neural Plast. *2016*, 1239629. https://doi.org/10.1155/2016/1239629.

134. Borges-Martins, V.P.P., Ferreira, D.D.P., Souto, A.C., Oliveira Neto, J.G., Pereira-Figueiredo, D., da Costa Calaza, K., de Jesus Oliveira, K., Manhães, A.C., de Melo Reis, R.A., and Kubrusly, R.C.C. (2019). Caffeine regulates GABA transport via A(1)R blockade and cAMP signaling. Neurochem. Int. *131*, 104550. https://doi.org/10.1016/j.neuint.2019.104550.

135. Yang, J.Y., Yang, G., Ren, J., Zhao, J., and Li, S. (2015). Caffeine suppresses GABA receptor-mediated current in rat primary sensory neurons via inhibition of intracellular phosphodiesterase. Neurophysiology *47*, 108–114. https://doi.org/10.1007/s11062-015-9505-4.

136. López-Moreno, J.A., Marcos, M., Calleja-Conde, J., Echeverry-Alzate, V., Bühler, K.M., Costa-Alba, P., Bernardo, E., Laso, F.J., Rodríguez de Fonseca, F., Nadal, R., et al. (2015). Histone Deacetylase Gene Expression Following Binge Alcohol Consumption in Rats and Humans. Alcohol Clin. Exp. Res. *39*, 1939–1950. https://doi.org/10.1111/acer.12850.

137. Pandey, S.C., Ugale, R., Zhang, H., Tang, L., and Prakash, A. (2008). Brain chromatin remodeling: a novel mechanism of alcoholism. J. Neurosci. *28*, 3729–3737. https://doi.org/10.1523/jneurosci.5731-07.2008.

138. Hranitz, J.M., Abramson, C.I., and Carter, R.P. (2010). Ethanol increases HSP70 concentrations in honeybee (Apis mellifera L.) brain tissue. Alcohol (Fayetteville, N.Y.) *44*, 275–282. https://doi.org/10.1016/j.alcohol.2010.02.003.

139. Koriyama, Y., Sugitani, K., Ogai, K., and Kato, S. (2014). Heat shock protein 70 induction by valproic acid delays photoreceptor cell death by N-methyl-N-nitrosourea in mice. J. Neurochem. *130*, 707–719. https://doi.org/10.1111/jnc.12750.

140. Abdelkader, T.S., Chang, S.N., Kim, T.H., Song, J., Kim, D.S., and Park, J.H. (2013). Exposure time to caffeine affects heartbeat and cell damage-related gene expression of zebrafish Danio rerio embryos at early developmental stages. J. Appl. Toxicol. *33*, 1277–1283. https://doi.org/10.1002/jat.2787.

141. Brunquell, J., Morris, S., Snyder, A., and Westerheide, S.D. (2018). Coffee extract and caffeine enhance the heat shock response and promote proteostasis in an HSF-1-dependent manner in Caenorhabditis elegans. Cell Stress Chaperones *23*, 65–75. https://doi.org/10.1007/s12192-017-0824-7.

142. Sharp, F.R., Butman, M., Aardalen, K., Nickolenko, J., Nakki, R., Massa, S.M., Swanson, R.A., and Sagar, S.M. (1994). Neuronal injury produced by NMDA antagonists can be detected using heat shock proteins and can be blocked with antipsychotics. Psychopharmacol. Bull. *30*, 555–560.

143. Chang, Y.F., Su, W.C., Su, C.C., Chung, M.W., Chang, J., Li, Y.Y., Kao, Y.J., Chen, W.P., and Daniels, M.J. (2022). High-Throughput Optical Controlling and Recording Calcium Signal in iPSC-Derived Cardiomyocytes for Toxicity Testing and Phenotypic Drug Screening. J. Vis. Exp. *178*, e63175. https://doi.org/10.3791/63175.

144. Hsiao, Y.H., Hsu, C.H., and Chen, C. (2016). A High-Throughput Automated Microfluidic Platform for Calcium Imaging of Taste Sensing. Molecules *21*, 896. https://doi.org/10.3390/molecules21070896.

145. Sullivan, E., Tucker, E.M., and Dale, I.L. (1999). Measurement of [Ca2+] using the Fluorometric Imaging Plate Reader (FLIPR). Methods Mol. Biol. *114*, 125–133. https://doi.org/10.1385/1-59259-250-3:125.

146. Volpato, V., Smith, J., Sandor, C., Ried, J.S., Baud, A., Handel, A., Newey, S.E., Wessely, F., Attar, M., Whiteley, E., et al. (2018). Reproducibility of Molecular Phenotypes after Long-Term Differentiation to Human iPSC-Derived Neurons: A Multi-Site Omics Study. Stem Cell Rep. *11*, 897–911. https://doi.org/10.1016/j.stemcr.2018.08.013.

147. Athreya, A.P., Armstrong, D., Gundling, W., Wildman, D., Kalbarczyk, Z.T., and Iyer, R.K. (2017). Prediction of Adenocarcinoma Development Using Game Theory (IEEE), pp. 1668–1671.

148. Ma, L., Xiao, Z., Li, K., Li, S., Li, J., and Yi, X. (2020). Game theoretic interpretability for learning based preoperative gliomas grading. Future Generat. Comput. Syst. *112*, 1–10. https://doi.org/10.1016/j.future.2020.05.038.

149. Topol, A., Zhu, S., Tran, N., Simone, A., Fang, G., and Brennand, K.J. (2015). Altered WNT Signaling in Human Induced Pluripotent Stem Cell Neural Progenitor Cells Derived from Four Schizophrenia Patients. Biol. Psychiatry *78*, e29–e34. https://doi.org/10.1016/j.biopsych.2014.12.028.

150. Narla, S.T., Lee, Y.W., Benson, C.A., Sarder, P., Brennand, K.J., Stachowiak, E.K., and Stachowiak, M.K. (2017). Common developmental genome deprogramming in schizophrenia - Role of Integrative Nuclear FGFR1 Signaling (INFS). Schizophr. Res. *185*, 17–32. https://doi.org/10.1016/j.schres.2016.12.012.

151. Brennand, K.J., Simone, A., Jou, J., Gelboin-Burkhart, C., Tran, N., Sangar, S., Li, Y., Mu, Y., Chen, G., Yu, D., et al. (2011). Modelling schizophrenia using human induced pluripotent stem cells. Nature *473*, 221–225. https://doi.org/10.1038/nature09915.

152. Shannon, P., Markiel, A., Ozier, O., Baliga, N.S., Wang, J.T., Ramage, D., Amin, N., Schwikowski, B., and Ideker, T. (2003). Cytoscape: a software environment for integrated models of biomolecular interaction networks. Genome Res. *13*, 2498–2504. https://doi.org/10.1101/gr.1239303.

153. Schindelin, J., Arganda-Carreras, I., Frise, E., Kaynig, V., Longair, M., Pietzsch, T., Preibisch, S., Rueden, C., Saalfeld, S., Schmid, B., et al. (2012). Fiji: an open-source platform for biological-image analysis. Nat. Methods *9*, 676–682. https://doi.org/10.1038/nmeth.2019.

154. Pedregosa, F., Varoquaux, G., Gramfort, A., Michel, V., Thirion, B., Grisel, O., Blondel, M., Prettenhofer, P., Weiss, R., and Dubourg, V. (2011). Scikit-learn: Machine learning in Python. J. Mach. Learn. Res. *12*, 2825–2830.

155. Kuleshov, M.V., Jones, M.R., Rouillard, A.D., Fernandez, N.F., Duan, Q., Wang, Z., Koplev, S., Jenkins, S.L., Jagodnik, K.M., Lachmann, A., et al. (2016). Enrichr: a comprehensive gene set enrichment analysis web server 2016 update. Nucleic Acids Res. *44*, W90–W97. https://doi.org/10.1093/nar/gkw377.

156. Bindea, G., Mlecnik, B., Hackl, H., Charoentong, P., Tosolini, M., Kirilovsky, A., Fridman, W.H., Pagès, F., Trajanoski, Z., and Galon, J. (2009). ClueGO: a Cytoscape plug-in to decipher functionally grouped gene ontology and pathway annotation networks. Bioinformatics *25*, 1091–1093. https://doi.org/10.1093/bioinformatics/btp101.

157. Stuart, T., Butler, A., Hoffman, P., Hafemeister, C., Papalexi, E., Mauck, W.M., Hao, Y., Stoeckius, M., Smibert, P., and Satija, R. (2019). Comprehensive Integration of Single-Cell Data. Cell *177*, 1888–1902.e21. https://doi.org/10.1016/j.cell.2019.05.031.

158. Plaisier, S.B., Taschereau, R., Wong, J.A., and Graeber, T.G. (2010). Rank-rank hypergeometric overlap: identification of statistically significant overlap between gene-expression signatures. Nucleic Acids Res. *38*, e169. https://doi.org/10.1093/nar/gkq636.

159. Chen, G., Yuan, P., Hawver, D.B., Potter, W.Z., and Manji, H.K. (1997). Increase in AP-1 transcription factor DNA binding activity by valproic acid. Neuropsychopharmacology *16*, 238–245. https://doi.org/10.1016/S0893-133X(96)00239-4.

160. Riss, J., Cloyd, J., Gates, J., and Collins, S. (2008). Benzodiazepines in epilepsy: pharmacology and pharmacokinetics. Acta Neurol. Scand. *118*, 69–86. https://doi.org/10.1111/j.1600-0404.2008.01004.x.

161. Tiwari, K.K., Chu, C., Couroucli, X., Moorthy, B., and Lingappan, K. (2014). Differential concentration-specific effects of caffeine on cell viability, oxidative stress, and cell cycle in pulmonary oxygen toxicity *in vitro*. Biochem. Biophys. Res. Commun. *450*, 1345–1350. https://doi.org/10.1016/j.bbrc.2014.06.132.

162. He, F., Liu, W., Zheng, S., Zhou, L., Ye, B., and Qi, Z. (2012). Ion transport through dimethyl sulfoxide (DMSO) induced transient water pores in cell membranes. Mol. Membr. Biol. *29*, 107–113. https://doi.org/10.3109/09687688.2012.687460.

163. Pham, H., Guan, M., Zoph, B., Le, Q., and Dean, J. (2018). Efficient Neural Architecture Search via Parameters Sharing (PMLR), pp. 4095–4104.

164. Metsalu, T., and Vilo, J. (2015). ClustVis: a web tool for visualizing clustering of multivariate data using Principal Component Analysis and heatmap. Nucleic Acids Res. *43*, W566–W570. https://doi.org/10.1093/nar/gkv468.

165. Lossi, L., Merighi, A., Novello, V., and Ferrandino, A. (2020). Protective Effects of Some Grapevine Polyphenols against Naturally Occurring Neuronal Death. Molecules *25*, 2925. https://doi.org/10.3390/molecules25122925.

166. Quintana, M., Saavedra, E., Del Rosario, H., González, I., Hernández, I., Estévez, F., and Quintana, J. (2021). Ethanol Enhances Hyperthermia-Induced Cell Death in Human Leukemia Cells. Int. J. Mol. Sci. *22*, 4948. https://doi.org/10.3390/ijms22094948.

167. Lu, P.Z., Lai, C.Y., and Chan, W.H. (2008). Caffeine induces cell death via activation of apoptotic signal and inactivation of survival signal in human osteoblasts. Int. J. Mol. Sci. *9*, 698–718. https://doi.org/10.3390/ijms9050698.

168. Ma, X.J., Wang, Y.S., Gu, W.P., and Zhao, X. (2017). The role and possible molecular mechanism of valproic acid in the growth of MCF-7 breast cancer cells. Croat. Med. J. *58*, 349–357. https://doi.org/10.3325/cmj.2017.58.349.

STAR★METHODS

KEY RESOURCES TABLE

REAGENT or RESOURCE	SOURCE	IDENTIFIER
Antibodies		
Mouse anti-human Nestin	EMD Millipore	Cat# MAB5326; RRID:AB_2251134
Mouse anti-human vimentin	Developmental Studies Hybridoma Bank	Cat# AMF-17b-c; RRID:AB_528505
Donkey anti-mouse IgG Alexa 488 -conjugated	Thermo Fisher Scientific	Cat# A21202; RRID:AB_141607
Chemicals, peptides, and recombinant proteins		
poly-L-ornithine	Sigma Aldrich	P4957-50ML
Mouse laminin	Invitrogen	23017015
TrypLE™ Express Enzyme (1X), no phenol red	Gibco	12604013
DMEM/F12	Gibco	11320033
N2 supplement	Gibco	17502048
B-27™ Supplement (50X), minus vitamin A	Gibco	12587010
FGF2	Peprotech	100-18B
GlutaMax	Gibco	35050061
Antibiotic-antimyotic	Gibco	15240062
Valproic acid	CalBiochem	676380
Diazepam	Sigma Aldrich	D0899
Ethanol	Fisher Scientific	T038181000
DMSO	Sigma Aldrich	D8418
ATP	Sigma Aldrich	A7699
Fluo4AM	Thermo Fisher Scientific	F23917
Caffeine	Sigma Aldrich	C0750
Critical commercial assays		
SMART-Seq v4 Ultra Low Input RNA Kit	TAKARA Bio	634890
Nextera XT DNA Library Prep Kit	Illumina	FC-131-1024
BioAnalyzer High Sensitivity DNA Kit	Agilent Technologies	5067-4626
Deposited data		
RNA sequencing results	This paper	GSE164499
Human NPC microarrays	Brennand et al.[54]	GSE40102 (GSM984925, GSM984826, and GSM984927)
All the codes for data analysis	This paper	https://github.com/BansalAnkush/Chemical-Effects-on-NPCs
Human iPSC-derived NPC transcriptome	Topol et al.[149]	GSE63738
Human iPSC-derived NPC transcriptome	Narla et al.[150]	GSE92874
Experimental models: Cell lines		
Human iPSC-derived neural progenitors	Brennand et al.[151]	AG09429 and GM03440
Software and algorithms		
Seurat	Satija Lab	v.3.0[152] https://satijalab.org/seurat/
Matlab	Mathworks	R2019a https://www.mathworks.com/products/matlab.html
FIJI	Schindelin et al.[153]	https://imagej.nih.gov/ij/
CellProfiler	Broad Institute	V4.2.6 https://cellprofiler.org/
Clampfit	Molecular Device	V10.7
Scikit	Pedregosa et al.[154]	https://scikit-learn.org/stable/
CytoScape	Shannon et al.[152]	V3.10.1 https://cytoscape.org/

(*Continued on next page*)

Continued		
REAGENT or RESOURCE	SOURCE	IDENTIFIER
EnrichR	Kuleshov et al.[155]	https://maayanlab.cloud/Enrichr/
ClueGO	Bindea et al.[156]	V2.5.10 https://apps.cytoscape.org/apps/cluego
Matlab tool box for calcium imaging analysis	Romano et al.[83]	https://www.mathworks.com/matlabcentral/fileexchange/72122-toolbox-romano-et-al
AutoML	Google	https://cloud.google.com/automl
ChemMine Tools	Backman et al.[105]	https://chemminetools.ucr.edu/
Random Forest (RF)	Pedregosa et al.[154]	https://github.com/BansalAnkush/Chemical-Effects-on-NPCs/tree/main/Scripts/Algorithms_Benchmarking
Gradient Boosting (GB)	Pedregosa et al.[154]	https://github.com/BansalAnkush/Chemical-Effects-on-NPCs/tree/main/Scripts/Algorithms_Benchmarking
Support Vector Machine (SVM)	Pedregosa et al.[154]	https://github.com/BansalAnkush/Chemical-Effects-on-NPCs/tree/main/Scripts/Algorithms_Benchmarking
Decision Tree (DT)	Pedregosa et al.[154]	https://github.com/BansalAnkush/Chemical-Effects-on-NPCs/tree/main/Scripts/Algorithms_Benchmarking
Prism	GraphPad	V9 https://www.graphpad.com/features
Other		
FV1000 T Confocal microscope	Olympus	
35mm glass bottom dish	Mat-tek	Cat # P35G-1.5-7-C
Apotome 2	Zeiss	

EXPERIMENTAL MODEL AND STUDY PARTICIPANT DETAILS

Culture of iPSC-derived NPCs

Two lines of human iPSC-derived NPCs D1 and D2 (originated from fibroblast lines AG09429 and GM03440 in,[151] respectively) were maintained in culture plates (Sarstedt, Nümbrecht, Germany) coated first with poly-L-ornithine (Sigma, St. Louis MO) then with mouse laminin (Invitrogen, Waltham, MA). The NPCs were lifted using TrypLE (Gibco, Waltham, MA) and passaged at a 1 to 3 ratio in the NPC medium, which contains DMEM/F12 (Gibco), antibiotic/antimyotic (1:100, Gibco), N2 supplement (1:100, Gibco), B27 without vitamin A (1:50, Gibco), GlutaMax (1:100, Gibco), and FGF2 (20 ng/ml, Peprotech, Cranbury, NJ). The NPCs were incubated at 37°C with 5% CO_2, and used for this study between passages 6 and 34 (Table S6).

METHOD DETAILS

Library preparation and bulk RNA-seq

Human NPCs (line D1) at passage 31 and D2 at passage 14 were trypsinized and pelleted in 1X PBS. These cells were not subjected to calcium imaging or chemical treatment. The cDNA libraries were prepared using the SMART-Seq v4 Ultra Low Input RNA Kit for Sequencing (TAKARA Bio, San Jose, CA) and Nextera XT DNA Library Prep Kit (Illumina, San Diego, CA) as per manufacturer's instructions. The unique barcode sequences were incorporated in the adaptors for multiplexed high-throughput sequencing. The final product was assessed for its size distribution and concentration using BioAnalyzer High Sensitivity DNA Kit (Agilent Technologies, Santa Clara, CA). The libraries were pooled and diluted to 3 nM using 10 mM Tris-HCl, pH 8.5, and then denatured using the Illumina protocol. The denatured libraries were loaded onto an S1 flow cell on an Illumina NovaSeq 6000 (Illumina) and run for 2X50 cycles according to the manufacturer's instructions. De-multiplexed sequencing reads were generated using Illumina bcl2fastq (v2.18.0.12) allowing no mismatches in the index read.

Bulk RNA-seq data analysis

Low quality reads from the RNA-seq dataset were removed via FastQC (using Sickle with the default setting). A HISAT2 index was built for the GRCm38 genome assembly using HISAT2 v2.1.0. RNA-seq reads of each sample were mapped using HISAT2 supplied with Ensembl annotation file GRCm38.78.gtf. For the count call, HTseq-count v0.10.0 was used. ClueGO (v2.5.10),[156] a plug-in of Cytoscape (v3.10.1)[152] was used for GO analysis. GOs with $p \leq 0.03$ were included in the data visualization. The parameters used were set to show only the pathways with $p \leq 0.03$ and kappa score = 0.4. GO tree interval was level 3 to 8. Redundant terms were fused using GO Term Fusion function to reduce the number of nodes.

Single cell RNA-seq

Nuclei of human NPCs were isolated using the Frankenstein protocol (https://res.cloudinary.com/dlg7p2kji/image/upload/v1574849709/customer-developed-protocols/frankenstein-protocol-for-nuclei-isolation-from-fresh-and-frozen-tissue.pdf). Briefly,

the NPCs (D2, passage 7-12) were trypsinized and pelleted, followed by lysis using Nuclei EZ Lysis kit (Sigma, St. Louis MO). Extracted nuclei were washed in 1X PBS containing 1.0% BSA and 0.2 U/μl RNase Inhibitor (Roche, Basel, Switzerland) and centrifuged at 500 RCF at 4°C. Pelleted nuclei were resuspended in lysis buffer and washed in wash buffer twice. The nuclei were strained using 40 μm cell strainer (BelArt, South Wayne, NJ). The sample was packed on ice and shipped to the sequencing facility equipped with the necessary equipment for processing (the prolonged storage on ice during shipment may be the reason for the low number of reads).

A single-cell RNA-seq library was prepared with the Chromium Single Cell 3' Library & Gel Bead Kit v3.1 (10x Genomics, Pleasanton, CA). NovaSeq 6000 (Illumina) was used to sequence 28 bases for Read 1, 91 bases for Read 2, and 8 bases for Index 1 read, respectively. The Cell Ranger 3.0.2 pipeline (10x Genomics, Pleasanton, CA) was used to make fastq files and align the reads to the GRCh38 reference genome. For the 19,759 nuclei detected, the mean Unique Molecular Identifier (UMI) per cell was 2,226. This value was used to filter out biased replicates. The mean numbers of total reads and genes were 9,969 per cell and 1,540 per cell, respectively. The UMI counts were analyzed using the Seurat R package v.3.0.[157] Read10X function was used to load the dataset. Low quality cells were removed using nFeature_RNA > 200 & nFeature_RNA < 7500 & percent.mt < 5. For global-scaling normalization, LogNormalize command was used with scale.factor = 10000. Highly variable features across cells were identified by considering the mean-variance relationship calculated using FindVariableFeatures function with selection.method = vst and nFeatures = 2000. ScaleData function was used for linear transformation of data. The pre-processing step was used to shift the expression of each gene so that the mean expression across all cells is 0. This step also ensures that highly expressed genes do not dominate. Principal component analysis was performed on the scaled data for variable features, and significant principal components (PC) were chosen using heuristic method called Elbow plot. FindNeighbors and FindClusters functions were used to cluster the cells. The variation among cells was visualized by UMAP on significant PCs. FindAllMarkers function was used for annotation of differentially expressed features across all clusters. The heat map of top 5 genes in each cluster was depicted across all cells using DoHeatmap function. Cell types representing each cluster were assigned based on literature search and analysis using Enrichr.[155] The GEO accession number for all data associated with this study is GSE164499.

Assessment of molecular profile similarity between NPC lines

Rank-rank hypergeometric overlap (RRHO) analysis was performed to evaluate the similarity of the transcriptomic profiles of NPCs at different passages using the algorithm provided in a previous study.[158] The top 1000 genes found in the bulk RNA-seq of D1 cells at passage 31 were compared to those of D2 cells at passage14. Spearman's correlation coefficient was calculated using the datasets of GSE92874 [150,151] and GSE63738 [149] by selecting the top 10 percent of genes which shows the highest standard deviations (SDs) across samples.

Chemical treatment of NPCs

Human NPCs were seeded onto 35 mm glass-bottom dishes (Mat-tek, Ashland, MA) coated as described above the day before imaging. Cells were incubated at 37°C with 5% CO2 in medium containing each chemical of interest under the following conditions based on known response times[159–161]: VPA (Calbiochem, Burlington MA): 1200 (H), 240 (M), and 48 (L) μM for 5.5 hours; DZM (Sigma-Aldrich, St. Louis, MO): 4400, 1100, and 275 nM for 5.5 hours; ETOH (Fischer Scientific, Waltham, MA): 60, 12, and 2.4 mM for 24 hours; CAF (Sigma-Aldrich, St. Louis, MO): 150, 30, and 6 μM for 4 hours. The DZM stock was prepared in DMSO at 2 mM, which was diluted for use in the NPC culture. NPCs exposed to the vehicle solution [i.e., cell culture medium (for VPA, ETOH, and CAF) or DMSO-containing cell culture medium (for DZM)] served as controls. The highest concentration of DMSO in the medium was 0.2% v/v, which has been shown to cause no significant changes in calcium dynamics *in vitro*.[162] We used cells from different passages to cover a broader range for each condition, but there was no strict criterion for passage selection. The passage numbers when cells were used in each experiment are shown in Table S6.

Calcium imaging

The culture medium containing each chemical of interest was aspirated, and the cells were loaded with 4.5 μM of Fluo4-AM (Thermo Fisher, Waltham, MA) in the NPC medium. The cells were then incubated for 20 minutes at 37°C with 5% CO2. Images were acquired using an Olympus FV1000 T confocal microscope (Olympus, Japan) for 5 minutes with a frame rate of 1 Hz (representative Videos in Videos S1, S2, S3, S4, S5, and S6). Spontaneous calcium activities were recorded first, and then cells were stimulated with ATP (Sigma-Aldrich, St. Louis, MO) at 20 μM to induce calcium responses. The same image acquisition settings were used in all sessions, and the center of the culture dish was imaged. One transient was plotted for the activity of each single cell throughout the entire recording session.

Immunocytochemistry

After calcium imaging human NPCs were fixed in 4% PFA in 1X PBS for 15 minutes at room temperature, rinsed with PBST (1X PBS with 0.1% Triton X-100) three times, and blocked with 2% BSA in PBST for 1 hour at room temperature. Nestin expression was visualized by using a mouse anti-human Nestin antibody (1:500, EMD MAB5326) and an anti-mouse Alexa 488 secondary antibody (ThermoFisher). Expression of Vimentin was visualized by using mouse anti-human Vimentin antibody (5 μg/mL, DSHB AMF-17b-c), followed by incubation with anti-mouse Alexa 488 antibody (ThermoFisher). Images were acquired using Apotome

2 (Zeiss, Oberkochen, Germany) and labeled cells were quantified using Cell Profiler 4.2.6 (Broad Institute, Cambridge, MA) and FIJI.[153] Expression of Nestin and Vimentin were evaluated in three independent experiments and single experiment, respectively. Two-tailed t-test with unequal variance was performed using Prism 9 (GraphPad) to determine whether the differences between D1 and D2 NPCs are significant.

Conversion of calcium activity traces to image files for machine learning with AutoML vision

Temporal traces of calcium activity in individual cells were contrast-enhanced and smoothened using FIJI and analyzed using the MATLAB toolbox described previously.[83] ROIs were defined by hexagon segmentation. The following parameters were used: frame frequency = 1 Hz, fluorescence decay time constant = 0.38 (default), minimal baseline-noise-scaled ΔF/F0 = 3. Slow-smooth dynamics option was used for threshold calculation, and Gaussian model was applied to calculate the noise. Dynamic threshold was used to process all 300 frames. One trace image file was extracted from each cell's calcium response over the 300 seconds. All traces were plotted individually (875 X 675 pixels) in JPEG format for AutoML Vision processing.

Feature extraction from calcium imaging data

The contrast-enhanced and smoothened image stacks described above were also used for extraction of features in calcium dynamics. The data of cells that showed a fluorescence intensity change larger than one standard deviation from the basal value were used. The change in fluorescence intensity was calculated as ΔF/F = (F(t)-F0)/F0, where the intensity of fluorescence signal at a given time point (F(t)) was normalized to the average during first five seconds (F0). The ΔF/F0 values were then plotted in Clampfit (v10.7, Molecular Devices, San Jose, CA), and the number of detectable calcium spikes (events), duration of events, event amplitude (ΔF/F0), area below event curve, max rise slope, and max decay slope were quantified using template detection function with user defined templates. Events with amplitude smaller than 0.2 were excluded during the event detection process.

t-distributed stochastic neighbor embedding (t-SNE) analysis

Trace images of calcium activity were used as input data. We used the sklearn.manifold.TSNE class from Scikit.[154] We tested the perplexity at the range of 5-500 with 1000-5000 iterations. All other parameters were as follows: n_components = 2, early_exaggeration = 12.0, learning_rate = 500.0, n_iter_without_progress = 300, min_grad_norm = 1e-7, metric = "euclidean", init = "random", verbose = 0, random_state = 42, method = 'barnes_hut', angle = 0.5.

Neural Architecture Search (NAS)

Deep learning models use NAS.[84] Before each epoch, the controller RNN builds a neural network architecture from all possible neural network architectures or the search space. This is done by following a search strategy, or a set of decisions to build these architectures, that iteratively seeks to maximize the output child CNN model's performance. NAS uses the Micro Search approach which makes it more robust and efficient for transfer learning as it learns from previous events.[84,163]

The controller learns via a policy gradient reinforcement learning paradigm, where the agent is the controller, the action is the decision taken by the controller to iteratively build (train and test) child CNN networks and the reward is the gap in expected vs actual performance of trained child CNN networks. The controller has a predetermined expectation of reward from a specific action, which is assigned a probability of p. The controller then learns the impact of its action from reward R, the gap between the expected performance and the actual performance of the child CNN network. This reward R is then used to update the controller's parameters for its search strategy so that it can generate better-performing child CNN networks in successive epochs. Underlying network structure is not visible from user in Google AutoML Vision.

AutoML vision model training

The training of the AutoML Vision model utilized full spectral traces from 300-second sessions without subdivision. Entire datasets of calcium traces were split into three groups: training (~70%), validation (~20%), and test (~10%) datasets. NAS algorithm under Google Cloud Platform (GCP) AutoML Vision was used for model training. Trace images were supplied to GCP AutoML Vision API and the three models for L, M, and H concentrations were trained separately. To reduce data variability, similar images were excluded automatically by AutoML Vision before the training process. For five-fold cross-validation, the same trace images were randomly re-assigned to the three parts using an in-house python script. Machine learning algorithms including Random Forest (RF), Gradient Boosting (GB), Support Vector Machine (SVM), and Decision Tree (DT) were used for benchmarking with default parameters.

Assessment of the bioactivity and physiochemical properties of chemicals by ChemMine tools

ChemMine tools was used to assess the similarity in bioactivity and physiochemical properties between VPA, DZM, ETOH, and CAF in silico.[105] Chemical structures were first downloaded from PubChem in SDF format and uploaded into the ChemMine online server. The structure of each chemical was tagged with its name, and then pairwise structural similarity analysis across all four chemicals was performed. After removing physiochemical features with zero values in all pairs of comparison, clustering analysis of chemicals by using the pairwise structural similarity score of physiochemical features was performed and visualized using ClustVis.[164]

QUANTIFICATION AND STATISTICAL ANALYSIS

Statistical analysis of features in calcium dynamics

Quantified values for each feature described above (except number of events) were averaged for each and subjected to statistical analysis using Prism (v9, GraphPad, San Diego, CA). The normality in data distribution was assessed by D'Agostino-Pearson test. Multiple comparisons between different experimental conditions were performed by nonparametric one-way ANOVA followed by Dunn's multiple comparison test. Statistical significance was defined as $p < 0.05$. Data were plotted as Boxplots, with the 25th to 75th percentiles represented by a box, the median by a line within the box, and the minimum and maximum values by whiskers. All data were presented as mean ± SEM. The number of cells analyzed for each tested condition is shown in Table S1 (from at least three independent experiments).

Performance metrics calculation

Precision, Recall, F scores and confusion matrix were used for evaluation of the model. Those scores were calculated as follows:

$$Precision = \frac{True\ Positive\ (TP)}{True\ Positive\ (TP)+False\ Positive\ (FP)} \quad \text{(Equation 1)}$$

$$Recall = \frac{True\ Positive\ (TP)}{True\ Positive\ (TP)+False\ Negative\ (FN)} \quad \text{(Equation 2)}$$

$$F1\ Score = 2\cdot\frac{Precision\cdot Recall}{Precision+Recall} \quad \text{(Equation 3)}$$

Confusion matrix.

	Predicted Label	
True Label	*True Positive (TP)*	*False Positive (FP)*
	False Negative (FN)	*True Negative (TN)*

Safety score and similarity matrix calculation

The safety score for each chemical at the defined concentrations was calculated as the average of percentages of false negatives (FNs), where the dataset of a chemical of interest was recognized as CONT in the 5-fold cross-validation. Safety scores for VPA, DZM, ETOH, and CAF at low concentrations can be denoted using Equations 4, 5, 6, and 7.

$$Safety\_Score_{VPA\_L} = VPA\_FN_{CONT\_L} \quad \text{(Equation 4)}$$

$$Safety\_Score_{DZM\_L} = DZM\_FN_{CONT\_L} \quad \text{(Equation 5)}$$

$$Safety\_Score_{ETOH\_L} = ETOH\_FN_{CONT\_L} \quad \text{(Equation 6)}$$

$$Safety\_Score_{CAF\_L} = CAF\_FN_{CONT\_L} \quad \text{(Equation 7)}$$

Here, $VPA\_FN_{CONT\_L}$, $DZM\_FN_{CONT\_L}$, $ETOH\_FN_{CONT\_L}$, and $CAF\_FN_{CONT\_L}$ represent the average percentages of images for VPA, DZM, ETOH, and CAF at the low concentration, respectively, that are classified as CONT. Similarly, safety scores were calculated for the high and medium concentrations (Table S7).

Weights for the results from different concentrations were defined based on the fold differences between concentrations (L, M, and H) for each chemical, and the linear correlation between biological phenotypes and the chemical concentrations as reported[165–168]: $w_L = 4^0$, $w_M = 4^1$, and $w_H = 4^2$.

The overall safety score for each chemical was calculated using Equations 8, 9, 10, and 11 with weights defined above. Here, $VPA\_FN_{CONT\_L}$, $VPA\_FN_{CONT\_M}$, and $VPA\_FN_{CONT\_H}$ are the percentages of VPA images classified as CONT. The percentages of DZM, ETOH, and CAF images classified as CONT are defined in the same way.

$$Safety\_Score_{VPA} = \frac{\left((w_L)VPA\_FN_{CONT\_L}\right)+\left((w_M)\ VPA\_FN_{CONT\_M}\right)+\left((w_H)\ VPA\_FN_{CONT\_H}\right)}{w_L+w_M+w_H} \quad \text{(Equation 8)}$$

$$Safety\_Score_{DZM} = \frac{((w_L)DZM\_FN_{CONT\_L})+((w_M)\ DZM\_FN_{CONT\_M})+((w_H)\ DZM\_FN_{CONT\_H})}{w_L+w_M+w_H} \quad \text{(Equation 9)}$$

$$Safety\_Score_{ETOH} = \frac{((w_L)ETOH\_FN_{CONT\_L})+((w_M)\ ETOH\_FN_{CONT\_M})+((w_H)\ ETOH\_FN_{CONT\_H})}{w_L+w_M+w_H} \quad \text{(Equation 10)}$$

$$Safety\_Score_{CAF} = \frac{((w_L)CAF\_FN_{CONT\_M})+((w_M)\ CAF\_FN_{CONT\_M})+((w_H)\ CAF\_FN_{CONT\_H})}{w_L+w_M+w_H} \quad \text{(Equation 11)}$$

The similarity matrix was similarly calculated utilizing the weighted average of percentages of false positives (FP) and FN obtained in the five-fold cross-validation as described below. w_L, w_M, w_H are the same as used for calculation of the safety score.

To define the similarity between VPA and DZM ($Similarity\_Index_{VPA\leftrightarrow DZM}$), average percentages of both FP and FN were considered for all the three concentrations as shown in Equation 12. It was calculated similarly for comparisons between VPA and ETOH ($Similarity\_Index_{VPA\leftrightarrow ETOH}$), VPA and CAF ($Similarity\_Index_{VPA\leftrightarrow CAF}$), DZM and ETOH ($Similarity\_Index_{DZM\leftrightarrow ETOH}$), DZM and CAF ($Similarity\_Index_{DZM\leftrightarrow CAF}$), and CAF and ETOH ($Similarity\_Index_{CAF\leftrightarrow ETOH}$) as shown in Equations 13, 14, 15, 16, and 17 (Table S8).

$$Similarity\_Index_{VPA\leftrightarrow DZM} = \left((w_L)\frac{VPA\_DZM\_FP_L+VPA\_DZM\_FN_L}{2}\right) + \left((w_M)\frac{VPA\_DZM\_FP_M+VPA\_DZM\_FN_M}{2}\right) + \left((w_H)\frac{VPA\_DZM\_FP_H+VPA\_DZM\_FN_H}{2}\right) \quad \text{(Equation 12)}$$

$$Similarity_{Index\,VPA\leftrightarrow ETOH} = \left((w_L)\frac{VPA_{ETOH_{FP}L}+VPA_{ETOH_{FN}L}}{2}\right) + \left((w_M)\frac{VPA\_ETOH\_FP_M+VPA\_ETOH\_FN_M}{2}\right) + \left((w_H)\frac{VPA\_ETOH\_FP_H+VPA\_ETOH\_FN_H}{2}\right) \quad \text{(Equation 13)}$$

$$Similarity\_Index_{VPA\leftrightarrow CAF} = \left((w_L)\frac{VPA\_CAF\_FP_L+VPA\_CAF\_FN_L}{2}\right) + \left((w_M)\frac{VPA\_CAF\_FP_M+VPA\_CAF\_FN_M}{2}\right) + \left((w_H)\frac{VPA\_CAF\_FP_H+VPA\_CAF\_FN_H}{2}\right) \quad \text{(Equation 14)}$$

$$Similarity\_Index_{DZM\leftrightarrow ETOH} = \left((w_L)\frac{DZM\_ETOH\_FP_L+DZM\_ETOH\_FN_L}{2}\right) + \left((w_M)\frac{DZM\_ETOH\_FP_M+DZM\_ETOH\_FN_M}{2}\right) + \left((w_H)\frac{DZM\_ETOH\_FP_H+DZM\_ETOH\_FN_H}{2}\right) \quad \text{(Equation 15)}$$

$$Similarity\_Index_{DZM\leftrightarrow CAF} = \left((w_L)\frac{DZM\_CAF\_FP_L+DZM\_CAF\_FN_L}{2}\right) + \left((w_M)\frac{DZM\_CAF\_FP_M+DZM\_CAF\_FN_M}{2}\right) + \left((w_H)\frac{DZM\_CAF\_FP_H+DZM\_CAF\_FN_H}{2}\right) \quad \text{(Equation 16)}$$

$$Similarity\_Index_{CAF\leftrightarrow ETOH} = \left((w_L)\frac{CAF\_ETOH\_FP_L+CAF\_ETOH\_FN_L}{2}\right) + \left((w_M)\frac{CAF\_ETOH\_FP_M+CAF\_ETOH\_FN_M}{2}\right) + \left((w_H)\frac{CAF\_ETOH\_FP_H+CAF\_ETOH\_FN_H}{2}\right) \quad \text{(Equation 17)}$$